Word count: 10584

Revision 1

Correlation between Si-Al disorder and hydrogen-bonding distance variation in ussingite ($Na_2AlSi_3O_8OH$) revealed by one- and two-dimensional multi-nuclear NMR and first-principles calculation

Xianyu Xue* and Masami Kanzaki

Institute for Planetary Materials, Okayama University, Yamada 827, Misasa, Tottori Japan

* Corresponding author; E-mail: xianyu@misasa.okayama-u.ac.jp

Tel: 81-858-43-3824

Submitted to Am Mineral 2023.3.23.

Revised 2023.5.17.

Abstract

Ussingite ($Na_2AlSi_3O_8OH$) is a mineral with a unique interrupted framework structure and strong hydrogen bonding. It contains 4-, 6- and 8- membered tetrahedral rings resembling feldspars, but, unlike the latter, is partially depolymerized. There are four crystallographically unique tetrahedral (T) sites, two of which (T1, T2) are Q^4 (i.e., having 4 next nearest neighbor (NNN) T sites), and the other two (T3, T4) are Q^3 (i.e., having 3 NNN T sites), each with NNN (in brackets) of T1(1T2, 1T3, 2T4), T2(1T1, 2T3, 1T4), T3(1T1, 2T2), T4(2T1, 1T2). There is one unique OH site in the T4-O8-H···O2-T3 configuration, where O8 and O2 are nonbridging oxygens (NBO). In the ordered structure,

T1 is fully occupied by Al, and the other three T sites by Si. Previous X-ray and neutron diffraction and ^{1}H and ^{29}Si NMR studies gave contradictory conclusions regarding Si-Al disorder. In this study, we were able to unambiguously clarify the issue via comprehensive one- and two-dimensional ^{1}H, ^{29}Si, ^{27}Al and ^{23}Na NMR and first-principles calculation. It was revealed that there is ~3% Si-Al disorder that occurs between neighboring T1-(O)-T2 site, such that the formation of Al-O-Al linkage and Al(Q^3) are avoided. The disorder was found to result in development of Si(Q^3) sites with a variety of NNN including 3Al and 3Si, and neighboring OH sites having significantly shorter and longer hydrogen-bonding distances than in the ordered structure, with ^{1}H chemical shifts near 15~16 ppm and 11 ppm, in addition to a main peak near 13.9 ppm. Good correlation was found between ^{1}H chemical shift, hydrogen-bonding (O-H, H···O and O···O) distances, and Si-O distances in the Si-O-H···O-Si linkage. This suggests that Si-Al disorder is correlated with variation in hydrogen-bonding distances via through-bond transmission of bond valence variations. This could be a universal phenomenon also applicable to other hydrous minerals. The revelation of preferential partition of Al in Q^4 over Q^3 sites to avoid the formation of Al-OH and Al-NBO provides insight into their behavior in other partially depolymerized hydrous aluminosilicate systems, such as glasses and melts.

Introduction

Ussingite ($Na_2AlSi_3O_8OH$) is a mineral characterized by a unique interrupted framework structure and strong hydrogen bonding (Fig. 1). It has been found in limited localities in the world, as a secondary mineral in pegmatite in the Lovozero and Khibina massifs of the

Kola Peninsula, Russia, in the Ilimaussaq intrusion, Greenland, and in sodalite xenoliths in an alkalic gabbro-syenite complex in Mont Saint-Hilaire, Canada. Its chemical composition has been reported to be close to the ideal formula (c.f., Anthony et al.).

The crystal structure of ussingite has been determined by single-crystal X-ray diffraction (XRD) (Rossi et al., 1974) and powder neutron diffraction (Williams and Weller, 2012). It has a space group P-1, Z=2 with lattice parameters: a = 7.2474(1) Å, b = 7.6813(1) Å, c = 8.6432(1) Å, α = 90.835(1)º, β = 99.771(1)º, γ = 122.581(1)º at 4 K (Williams and Weller, 2012). The structure contains 4-, 6- and 8- membered tetrahedral rings resembling feldspars, but, unlike the latter, is partially depolymerized. There are nine crystallographically unique oxygen sites, seven of which are bridging oxygens that each link two tetrahedral (T) cations, and the remaining two (O2, O8) are nonbridging oxygens (NBO) that each bond to one T cation and to one H via O-H or H···O bond. The bulk NBO/T (NBO per tetrahedral cation), a parameter describing the degree of depolymerization of the system, is 0.5. There are four T sites, two of which (T1, T2) are Q^4 (i.e., having 4 next nearest neighbor (NNN) T sites), and the other two (T3, T4) are Q^3 (i.e., having 3 NNN T sites). Their NNN environments (in brackets) are T1(1T2,1T3,2T4), T2(1T1,2T3,1T4), T3(1T1,2T2), T4(2T1,1T2), so that the T3/T4 sites are not NNN to one another, but are each surrounded by three T1/T2 sites. There is only one unique H site located in the T4-O8-H···O2-T3 linkage, with O8-H, H···O2 and O8···O2 distances of 1.070(8), 1.412(7) and 2.481(5) Å at 4 K (Williams and Weller, 2012).

The crystal structure of ussingite from X-ray diffraction (Rossi et al., 1974) did not show any Si-Al disorder. In the ordered structure, T1 is occupied by Al, and the other T sites by Si. Possibility of Si-Al disorder was suggested by Ribbe (1974), who noted that exchange

of 5% of Al in T1 site with Si in T3 site resulted in better fit to an empirical equation for T-O bond distances. Oglesby and Stebbins (2000) reported ^{29}Si MAS and ^{1}H-^{29}Si CP (cross polarization) MAS NMR results for ussingite, and attributed three observed peaks at -96.5, -87.7 and -83.8 ppm to the T2, T3 and T4 sites of the ordered structure. No indication of disorder was shown. Johnson and Rossman (2004) reported ^{1}H MAS NMR spectra for ussingite that contain a main peak near 13.9 ppm and two smaller peaks around 15.9 ppm and 11.0 ppm. It is well known that the ^{1}H chemical shift is correlated with hydrogen-bonding distance. The authors noted that the main peak is close to that expected from the ordered structure. They interpreted the peak near 15.9 ppm to be a result of Si-Al disorder between T1 and T3 site as suggested by Ribbe (1974), but could not assign the 11.0-ppm peak. Williams and Weller (2012), however, reported that the structure from powder neutron diffraction shows no disorder in Si-Al distribution or H position. Thus, previous studies gave contradictory conclusions regarding Si-Al disorder in ussingite.

The aim of this study was twofold: The first was to completely clarify the state of Si-Al disorder and how it is related to hydrogen-bonding distance variation in ussingite via a comprehensive one- (1D) and two-dimensional (2D) multi-nuclear NMR measurement and first-principles calculation. The second was to use ussingite as a model compound to gain a general crystal chemical understanding of (1) the partition behavior of Al/Si and nature of OH in partially depolymerized aluminosilicate systems, and (2) the relationship between Si-Al disorder and hydrogen-bonding distance variation. Previous studies of partially depolymerized anhydrous and hydrous aluminosilicate glasses have suggested that Al tends to partition into Q^4 species than less polymerized Q^3 species (e.g., Allwardt et al., 2003; Neuville et al., 2004; Xue and Kanzaki, 2008). In prehnite ($Ca_2Al^{VI}(Al^{IV}Si_3)O_{10}(OH)_2$), a

mineral containing mixed Q^4 and Q^2 sites, tetrahedral Al (Al^{IV}) was also found to preferentially partition into Q^4 site (Stebbins, 1992). If the proposed Si-Al disorder between T1 and T3 site in ussingite were valid, it would imply the existence of unfavorable Al(Q^3). Insight into the relationship between Si-Al disorder and hydrogen-bonding distance is also of broad interest, because the latter is an important factor governing the physical properties of minerals, and many hydrous silicate minerals show Si-Al disorder.

Experimental and Calculation Methods

Sample description and characterization

Two ussingite samples were examined: Sample one (purchased from Mineral Street) was from Alluaiv Mt, Lovozero, Kola Peninsula, Russia. Sample two (purchased from eBay) was described as from Greenland. Both samples are fine-grained polycrystalline aggregates of ussingite with a pale purple color (see supplementary Fig. 1s). A portion of each sample was powdered for XRD and NMR measurements. Raman and electron microprobe (EPMA) measurements were also made on selected fragments. The powder XRD, Raman, EPMA and NMR measurements all revealed only ussingite phase.

The chemical composition of ussingite was quantitatively analyzed using a JEOL JXA-8530F field-emission electron microprobe (FE-EPMA). An accelerating voltage of 15 kV, a low beam current of 1 nA and a beam diameter of 10 μm was used to minimize damage to the sample. The resultant compositions for both samples are within uncertainty of the ideal formula (see Table 1). The water content of ussingite in sample 1 was also estimated by ^1H

MAS NMR to be 3.1(1) wt%, which agrees well with that (2.98 wt%) expected from the ideal formula.

The Raman spectra in the high-frequency region exhibit broad bands with at least three maxima (1800~1870, 2390, 2620 cm^{-1}), which is typical of strong hydrogen bonding (see supplementary descriptions and Fig. 2s for details).

NMR spectroscopy

NMR measurements were performed on a standard-bore Bruker 9.4 T Avance NEO NMR spectrometer, using a 3.2 mm (for ^{1}H and ^{29}Si) or 1.9 mm (for ^{23}Na and ^{27}Al) HX MAS probe. The chemical shifts for ^{1}H and ^{29}Si were referenced externally to tetramethylsilane (TMS); those for ^{23}Na and ^{27}Al were referenced, respectively, to 1M NaCl solution and 1M $Al(NO_3)_3$ solution, all reproducible to better than about ± 0.1 ppm.

Detailed pulse sequences, spin-lattice relaxation time constants (T_1) measured, and acquisition and processing parameters for the reported NMR spectra can be found in supplementary Figure 3s and Tables 1s and 2s. Only an outline is described below.

^{1}H MAS NMR spectra were obtained at a range of spinning rates up to 24 kHz with a sufficiently long recycle delay of 400 s (sample 1) or 150~300 s (sample 2), using the DEPTH2 sequence (Cory and Ritchey, 1988) for background suppression. The ^{1}H T_1 were found to be 44~81 s and 28~45 s for peaks of ussingite in sample 1 and 2, respectively.

Single-pulse ^{29}Si MAS NMR spectra were obtained at a spinning rate of 20 kHz using a 1.8 μs-pulse (45° flip angle) and a recycle delay time of 4500 s, with proton decoupling using the swept-frequency-TPPM sequence (Thakur et al., 2008). The long recycle delay was used because of long ^{29}Si T_1 (7630~11750 s).

^{1}H-^{29}Si CP MAS NMR spectra were acquired for both samples at a spinning rate of 10 kHz and a range of contact times from 1 to 20 ms. A recycle delay of 150 s (sample 1) or 60 s (sample 2) with swept-frequency-TPPM proton decoupling during acquisition were used.

2D ^{1}H-^{29}Si HETCOR spectrum was obtained for sample 1 using the efficient ^{1}H→^{29}Si→^{1}H double CP MAS technique (Ishii and Tycko, 2000) at a spinning rate of 24 kHz with a relaxation delay of 100 s. No decoupling was applied.

2D rotor-synchronized ^{1}H double-quantum (DQ) MAS NMR spectrum was acquired on sample 1 using the POST-C7 scheme (Hohwy et al., 1998) at a spinning rate of 14.7 kHz and recycle delay of 100 s, with a DQ excitation/reconversion duration of 408 μs each.

^{27}Al and ^{23}Na MAS NMR spectra were acquired at a spinning rate of 20 kHz with a pulse width of 0.3 μs (^{27}Al) or 0.4 μs (^{23}Na) (both about 30° tip angle for selective central transition) and a recycle delay time of 2 s. No proton decoupling was applied. Spectrometer deadtime (~6.5 μs) resulted in a rolling baseline, which was improved by linear prediction. For ^{27}Al, a further spline baseline correction was also applied.

High-resolution 2D rotor-synchronized ^{27}Al and ^{23}Na triple-quantum (3Q) MAS NMR spectra were obtained for both samples at a spinning rate of 20 kHz and recycle delay time of 20~26 s (^{27}Al) or 30 s (^{23}Na) using the efficient SPAM (soft-pulse added mixing)-3QMAS pulse scheme (Amoureux et al., 2005; Gan and Kwak, 2004). No decoupling was applied. The chemical shift reference in the isotropic dimension follows the universal scaling convention of Amouroux and Fernandez (1998).

Simulation of the NMR spectra was performed using the SOLA program in the Bruker Topspin 4.1.4. package.

161

162 **First-principles calculation**

163 First-principles density functional theory calculations of energy and NMR parameters
164 were performed using the Quantum-ESPRESSO (QE) package (version 7.0)(Giannozzi et
165 al., 2017; Giannozzi et al., 2009), similar to our previous studies (Kanzaki and Xue, 2016;
166 Xue et al., 2017). Both the ordered ussingite structure of ideal composition (Z=2, 32 atoms
167 in one unit cell) and models for Si-Al disorder were studied. For the latter, models for one
168 pair of Al-Si exchanged between a T1 site and each of its NNN (1T2, 1T3, 2T4), as well as
169 between a pair of remote T1 and T2 site in a 2 × 2 × 2 supercell (containing 16 formulae
170 and 256 atoms) were examined. This corresponds to 6.25% (1/16) of the Al exchanged with
171 Si. The size of the 2 × 2 × 2 supercell was found to be sufficient to produce isolated
172 disordered structure.

173 For each calculation, the structure (both cell parameters and atomic coordinates) was
174 first relaxed at 1 bar using the PWscf code of the QE package. NMR chemical shielding
175 and electric field gradient (EFG) tensors were then calculated using the Gauge-Including
176 Projector-Augmented Wave (GIPAW) method (Pickard and Mauri, 2001) implemented in
177 the QE-GIPAW package (version 7.0). The PBEsol functional within the generalized
178 gradient approximation (GGA) for the exchange-correlation energy (Perdew et al., 1996;
179 Perdew et al., 2008) and the following PAW-pseudopotentials from the PSlibary (Dal
180 Corso, 2014) were used for both calculations: Si.pbesol-n-kjpaw_psl.0.1.UPF, Al.pbesol-n-
181 kjpaw_psl.0.1.UPF, O.pbesol-n-kjpaw_psl.0.1.UPF, Na.pbesol-spn-kjpaw_psl.0.2.UPF,
182 H.pbesol-kjpaw_psl.0.1.UPF). A Monkhorst-Pack grid of 2 × 2 × 2 for the Brillouin zone
183 sampling was used for the ordered ussingite, and a comparable grid size of 1 × 1 × 1 was

used for models of 2 × 2 × 2 supercell with Al-Si disorder. A kinetic energy cutoff (ecutwfc) of 50 Ry and a charge density cutoff (ecutrho) of 300 Ry, and SCF energy convergence threshold of 10^{-14} Ry were used for all the reported data.

In order to test whether these parameters were sufficient, we also performed test calculations on ordered ussingite using a finer grid of 4 × 4 × 4 at ecutwfc from 50 to 80 Ry in step of 10 Ry, with ecutrho set to six times of ecutwfc. The calculation results with parameters above differ from that with a higher ecutwfc of 80 Ry by ≤ 0.1 ppm in ^{1}H, ^{29}Si and ^{27}Al chemical shielding (σ_i), by ≤ 0.03 MHz for ^{23}Na and ^{27}Al quadrupolar coupling constant (C_Q), and by ≤ 0.02 for ^{23}Na and ^{27}Al electric field gradient (EFG) asymmetry parameter (η_Q), but by 3~4 ppm for σ_i^{Na}. The difference in σ_i^{Na} between the two Na sites differs by 0.2 ppm. Thus, the results were satisfactory for all but σ_i^{Na}, and still the difference in σ_i^{Na} between different Na sites might still be useful.

Our previous study for similar calculation on several silicate minerals showed that experimental ^{29}Si and ^{1}H chemical shifts (δ_i^{Si}, δ_i^{H}) were reproduced within ±2 and ±1 ppm or better for tetrahedral Si and OH, respectively, with agreement in relative difference generally better for local structures of greater similarity (Xue et al., 2017). In this study, we also performed calculation for low-albite ($NaAlSi_3O_8$, space group P-1 (Smith et al., 1986)) in the same way as for ussingite, using a grid of 2 × 2 × 2, for comparison. We have referenced δ_i^{Si} and δ_i^{H} to ordered ussingite (using the strongest peak in the experimental NMR spectra) to focus on variations brought about by Si-Al disorder. This yielded calculated δ_i^{Si} for low-albite that differ from the experimental values (Sanchez-Munoz et al., 2022) by -1.2~-3.3 ppm. The δ_i^{Al} and δ_i^{Na} were referenced to the experimental value for

This is the peer-reviewed, final accepted version for American Mineralogist, published by the Mineralogical Society of America.
The published version is subject to change. Cite as Authors (Year) Title. American Mineralogist, in press.
DOI: https://doi.org/10.2138/am-2023-9008. http://www.minsocam.org/

low-albite (δ_i^{Al}: 63.0 ppm, δ_i^{Na}: -8.95 ppm (=average of two values (-8.7, -9.2 ppm) obtained at magnetic fields of 9.4 and 19.6 T)(Sanchez-Munoz et al., 2022).

Results

^{29}Si MAS and ^{1}H-^{29}Si MAS NMR. The ^{29}Si MAS NMR spectrum of sample 1, obtained at a spinning rate of 20 kHz with swept-frequency-TPPM proton decoupling, contains three main peaks near -84.1, -87.9 and -96.5 ppm, with the two peaks near -84.1 and -96.5 ppm much broader (Fig. 2). The signal to noise (S/N) ratio of the spectrum is relatively poor, despite long acquisition time (~10 days) due to long ^{29}Si T_1.

^{1}H-^{29}Si CP MAS NMR spectra acquired at contact times from 1 to 20 ms at a spinning rate of 10 kHz were found to give increasing intensities for all peaks with contact time. Only the spectra at a contact time of 20 ms are shown, which are similar for the two samples (Fig. 2). Like the ^{29}Si MAS NMR spectrum, the ^{1}H-^{29}Si CP MAS NMR spectra also contain three main peaks near -84.1, -87.9 and -96.5 ppm. The peak near -87.9 ppm was found to be particularly sensitive to proton decoupling, and narrower peak width was obtained with the swept-frequency-TPPM decoupling scheme than CW (continuous wave) or TPPM decoupling. The better S/N ratio of the CP spectra allowed smaller features to be clearly revealed. The peak near -84.1 ppm clearly contain multiple components, that near -96.5 ppm exhibits splitting, and all three main peaks each contain a low-frequency tail. Furthermore, there are also two small, well-resolved peaks near –81.0 and -91.6 ppm (Fig. 2).

The well-established empirical correlation between δ_i^{Si} and Q^n and the Al/Si constituents in their NNN (c.f., Kirkpatrick, 1988; Stebbins and Xue, 2014) suggests that the three groups of main peaks near -84.1, -87.9 and -96.5 ppm can each be attributed to Q^3(1Si,2Al), Q^3(2Si,1Al) and Q^4(3Si,1Al), as are expected for the T4, T3 and T2 sites in the ordered structure of ussingite, and also assigned by Oglesby and Stebbins (2000). The two weaker peaks near –81.0 and -91.6 ppm can be attributed to Q^3(3Al) and Q^3 (3Si), respectively. These assignments are in agreement with first-principles calculation result described below.

Oglesby and Stebbins (2000) also reported ^{29}Si MAS and ^{1}H-^{29}Si CP MAS NMR spectra for ussingite, but could not observe features other than three main peaks, with the two peaks of Q^3 partially overlapping. The broader peak widths of their spectra could have been caused by dipolar coupling, because they were measured at a lower spinning rate of 2.5~3 kHz, and no proton decoupling seems to have been applied.

The ^{1}H-^{29}Si CP spectra with the longest contact times of 12 and 20 ms were simulated to obtain relative abundances among Q^3 sites. Although CP in general yields relative intensities that are dependent on the relative Si-H distances, the different Q^3 sites are expected to have similar CP dynamics (Oglesby and Stebbins, 2000). Their relative intensities in the CP spectra with contact times of 12 and 20 ms were found to be close to each other, and also close to that of the ^{29}Si MAS NMR spectrum (in which only the two main Q^3 peaks are clearly recognizable), suggesting it is a reasonable approximation. The simulation was made utilizing information from 2D ^{1}H-^{29}Si HETCOR spectrum (described below), in which different components are better resolved, and included 17 pseudo-Voigt components: one for Q^3(3Al), seven for Q^3(1Si,2Al), three for Q^3(2Si,1Al), one for Q^3(3Si), and five for Q^4(3Si,1Al) (see supplementary Fig. 4s and Table 3s for an example).

Simulation for the central band region only and that also including the weak spinning sidebands were both performed, and gave similar relative abundances. Only the former is reported in Table 2.

^{1}H MAS and 2D ^{1}H DQ MAS NMR. ^{1}H MAS NMR spectra of sample 1 and 2 acquired at a range of spinning rates from 5 to 24 kHz all contain a main peak near 13.9 ppm with a small low-frequency shoulder near 13.3 ppm, a group of three partially resolved peaks with approximately 1:2:1 intensity ratio in the range of 15~16 ppm, and another weaker peak near 11.1 ppm (see Figure 3 for the spectra at 24 kHz). The peak widths of all peaks become narrower at higher spinning rates, indicating line broadening due to ^{1}H-^{1}H dipolar coupling. They are overall broader for sample 2 than sample 1 at a given spinning rate, which could be due to different level of paramagnetic impurities. There is also another weak peak near 4.4 ppm, which has a much shorter T_1 (< 5 s) than the other peaks, and also loses intensity after extensive sample spinning, suggesting it is due to surface-absorbed water. These ^{1}H MAS NMR spectra overall resemble, but have better resolution than, those reported by Johnson and Rossman (2004) at lower spinning rates (6 and 12 kHz). From hereafter, only peaks in the 11 to 16 ppm range will be described.

The ^{1}H MAS NMR spectra were simulated using 7 pseudo-Voigt components: four in the 15~16 ppm range (as revealed by 2D ^{1}H-^{29}Si HETCOR spectrum described below), two for the main peak near 13.9 ppm and its shoulder, and one near 11 ppm (see supplementary Fig. 5s and Table 4s for an example). Simulation for the central band region only and that also including weak spinning sidebands were both performed and yielded similar relative abundances. Only the former is reported in Table 3.

Information about the relative ^{1}H -^{1}H proximity was obtained from 2D ^{1}H DQ MAS NMR spectrum for sample 1 (Fig. 4a). A spin pair that experience dipolar coupling (as a result of spatial proximity) will yield two peaks with a DQ frequency in the F_1 dimension equal to the sum of their respective frequencies in the F_2 dimension. Peaks between two spins of different frequencies will be referred to as cross peaks, and those of equal frequencies as diagonal peaks. In addition to a diagonal peak for the strongest ^{1}H peak near 13.9 ppm, cross peaks between the main peak near 13.9 ppm and each of the other peaks (three partially resolved peaks in the 15~16 ppm range and the 11 ppm-peak) are clearly recognized. Weaker cross peaks among peaks in the 15~16 ppm range, and weaker cross peak between the 11 ppm and 15~16 ppm peaks are also present. This indicates all the observed peaks arise from protons in the same phase (ussingite).

2D ^{1}H-^{29}Si HETCOR. The 2D ^{1}H-^{29}Si HETCOR spectrum acquired for sample 1 at a spinning rate of 24 kHz and a contact time of 8 ms is shown in Figure 5a. It provides information about relative H-Si proximity. Peaks will be observed only between ^{1}H and ^{29}Si spin pairs that are dipolar coupled due to close proximity. All the observed ^{29}Si peaks are found to be correlated with one or more of the ^{1}H peaks attributable to ussingite, suggesting they all arise from Si in the ussingite structure. As the ideal ordered structure is expected to produce only three ^{29}Si peaks, this is a clear indication of deviation from the ideal ordered structure. Furthermore, because T3/T4 sites only have NNN of T1/T2, the observation of ^{29}Si peak of Q^3(3Al) can be achieved only if some Al are transferred from T1 to T2 site, but cannot be accounted for by disorder between T1 and T3 site as suggested previously. The symmetric development of ^{29}Si peaks of both Q^3(3Al) and Q^3(3Si), which

297 requires extra Al in T2 site and extra Si in T1 site simultaneously, suggests that these peaks
298 arise from Si-Al disorder (exchange) between T1 and T2 site, rather than deviation in
299 stoichiometry (excess Si or Al), consistent with the EPMA result.
300 The spatial relationship between the different H and Si sites is revealed by the specific
301 correlations in the 2D ^{1}H-^{29}Si HETCOR spectrum. We will focus on ^{29}Si peaks of Q^3 (-80
302 to -92 ppm), as OH is located in between a T4 and T3 site. It can be recognized from Figure
303 5a that the strongest ^{1}H peak, near 13.9 ppm, exhibits cross peaks with the two main ^{29}Si
304 peaks near -84.1 and -87.9 ppm that are attributable to Q^3(1Si,2Al), Q^3(2Si,1Al),
305 respectively. This is in accord with the configuration T4(1Si,2Al)-OH···O-T3(2Si,1Al) in
306 the ordered structure. The group of ^{1}H peaks at 15 ~ 16 ppm can be clearly recognized to
307 consist of four peaks in the 2D spectrum: Two of them each correlate only with one or two
308 weak ^{29}Si peaks that contribute to shoulders of the main peak near -87.9 ppm (attributable
309 to Q^3(2Si,1Al)), and the other two are each correlated only with two weak ^{29}Si peaks that
310 contribute to shoulders of the main peak near -84.1 ppm (attributable to Q^3(1Si,2Al)). The
311 ^{1}H peak near 11 ppm shows cross peaks with two weak ^{29}Si peaks near –81.0 and -91.6
312 ppm, which are attributable to Q^3(3Al) and Q^3(3Si), respectively. Therefore, one of the
313 correlated Si for each of the four ^{1}H peaks near 15~16 ppm has NNN different from those
314 of T3/T4 in the ordered structure (i.e., one Q^3(2Si,1Al) and one Q^3(1Si,2Al)), and both of
315 the correlated Si for the ^{1}H peak near 11 ppm differ from the latter, and thus must be NNN
316 to T sites with Si-Al disorder. Again, as T3/T4 sites only have NNN of T1/T2, this is
317 consistent with Si-Al disorder between T1 and T2 site. Furthermore, because the single T2
318 NNN of T4 and single T1 NNN of T3 in the T4(2T1,1T2)-OH···O-T3(1T1,2T2) linkage
319 are linked to each other via BO (see further descriptions below), the cross peaks of ^{29}Si

This is the peer-reviewed, final accepted version for American Mineralogist, published by the Mineralogical Society of America.
The published version is subject to change. Cite as Authors (Year) Title. American Mineralogist, in press.
DOI: https://doi.org/10.2138/am-2023-9008. http://www.minsocam.org/

320 Q^3(3Al) and Q^3(3Si) with a common proton can only arise from Si-Al exchange between
321 neighboring T1-(O)-T2 site.

322 The correlations for the five ^{1}H peaks related to disorder can be summarized as below
323 (also labelled in Fig. 5a):

324 1. (^{1}H) 15.8 ppm - (^{29}Si) -83.1 & -85.5 ppm: Q^3(1Si,2Al)-(OH···O)-Q^3(1Si,2Al)

325 2. (^{1}H) 15.47 ppm - (^{29}Si) -83.3 & -85.0 ppm: Q^3(1Si,2Al)-(OH···O)-Q^3(1Si,2Al)

326 3. (^{1}H) 15.54 ppm - (^{29}Si) -88.6 & -88.6 ppm: Q^3(2Si,1Al)-(OH···O)-Q^3(2Si,1Al)

327 4. (^{1}H) 15.1 ppm - (^{29}Si) -87.9 & -89.3 ppm: Q^3(2Si,1Al)-(OH···O)-Q^3(2Si,1Al)

328 5. (^{1}H) 11.1 ppm - (^{29}Si) -81.0 & -91.6 ppm: Q^3(3Al)-(OH···O)-Q^3(3Si)

329 The hydrogen bond (O-H···O) has been shown in bracket above, because the ^{1}H-^{29}Si
330 HETCOR spectrum alone cannot distinguish between Si-OH and Si-O···H due to the
331 relatively strong hydrogen bonding. Nevertheless, this information can be gained from
332 comparison with first-principles calculation result (see below).

333

334 **^{27}Al MAS and 2D 3QMAS NMR.** The ^{27}Al MAS and 3QMAS NMR spectra of sample
335 1 are shown in Figures 6 and 7, respectively. Those of sample 2 are similar (not shown). In
336 the ordered structure of ussingite, Al occupies only T1 site. Both the central band and
337 spinning sidebands of the ^{27}Al MAS NMR spectrum can be reasonably (though not
338 perfectly) simulated with a single set of parameters (δ_i^{Al}, C_Q^{Al}, and η_Q^{Al})(see Table 4 and
339 Fig. 6), although a larger line broadening is required for the central band than the spinning
340 sidebands. However, the 2D 3QMAS NMR spectrum exhibits somewhat varying MAS
341 peak shapes at different isotropic peak positions (Fig. 7). The projection in the isotropic
342 dimension is also somewhat asymmetric with a small high-frequency tail. These spectral

features indicate the presence of some distribution of NMR parameters, consistent with local structural disorder around Al. No further attempt will be made to evaluate quantitatively their distribution.

^{23}Na MAS and 2D 3QMAS NMR. The ^{23}Na MAS and 3QMAS NMR spectra of sample 1 are shown in Figure 8. Those of sample 2 are similar (not shown). In the ordered structure of ussingite, there are two Na sites, with Na1 in six coordination and Na2 in five coordination. The 2D 3QMAS NMR spectrum revealed two well resolved peaks in the isotropic dimension, consistent with the presence of two Na sites (Fig. 8a). The MAS projections of these two peaks were each simulated with a single set of parameters to best reproduce both the peak maximum position in the isotropic dimension (δ_1^{Na}), and positions of discontinuities (e.g., peak maxima and shoulders) in the MAS projection (see Fig. 8b, Table 4). The central band of the 1D ^{23}Na MAS NMR spectrum was also reasonably, though not perfectly, simulated with these two sets of parameters (see Fig. 8b). Among the two peaks, the one with smaller δ_i^{Na} may be attributed to Na1, according to the known correlation between δ_i^{Na} and Na coordination number (cf. Xue and Stebbins, 1993), which is consistent with first-principles calculation result described below. However, the MAS projections for the two peaks in the 2D 3QMAS NMR spectrum clearly both deviate from the peak shape for a single site (see Fig. 8b), suggesting a distribution of NMR parameters due to local structural disorder. No further attempt will be made to evaluate quantitatively their distribution.

First-principles calculation results

366 **Geometry and energy of relaxed structures.** The relative energies and unit-cell
367 volumes at 0 K of fully relaxed structures for the ideal ordered ussingite and five disorder
368 models that each contain one Al exchanged with a Si in a different site in a 2 × 2 × 2
369 supercell are listed in Table 5. The calculated unit-cell volumes for the ordered structure
370 and five disorder models only differ slightly, and are larger than that from X-ray diffraction
371 under ambient condition (Rossi et al., 1974) and neutron diffraction at 4 K (Williams and
372 Weller, 2012) by 0.3~0.4% and 1.1~1.2%, respectively. Among the five disorder models,
373 model 1 (Si-Al exchange over T1-O-T2) gave the lowest energy that is 28~69 kJ/mol lower
374 than models 2 to 5. Therefore, model 1 is energetically the most favorable and thus most
375 plausible model.

376 As mentioned in the Introduction, previous studies of partially depolymerized
377 aluminosilicate glasses indicated Al tends to partition into Q^4 species than less polymerized
378 Q^3 species. Also, the formation of Al-O-Al linkage has been known to be energetically
379 unfavorable (Al avoidance principle) (Lowenstein, 1954). Among the five disorder models,
380 model 1 is the only one that yields no energetically unfavorable Al-O-Al linkage or Al(Q^3).
381 Model 5 for Si-Al exchange between two remote T1-T2 site results in Al-O-Al linkage.
382 Models 3 and 4 for Si-Al exchange over T1-O-T4 result in both Al-O-Al and Al(Q^3)-OH.
383 Model 2 for Si-Al exchange over T1-O-T3 is somewhat counter-intuitive: Although a
384 simple Si-Al exchange would result in Al(Q^3)-NBO, after structural relaxation, Al(Q^3)-OH
385 was produced instead, because H shifted to become closer to Al (also see below). Thus, the
386 trend in energy for the five disorder models is consistent with the known tendency of less
387 favorable development of Al-O-Al and preference of Al for Q^4 than Q^3 site.

This is the peer-reviewed, final accepted version for American Mineralogist, published by the Mineralogical Society of America.
The published version is subject to change. Cite as Authors (Year) Title. American Mineralogist, in press.
DOI: https://doi.org/10.2138/am-2023-9008. http://www.minsocam.org/

To facilitate understanding of the calculated NMR parameters, below we examine how the Si-Al disorder affects the local environments of Si, Al and OH for disorder model 1.

Si-Al exchange over one T1-O-T2 alters the NNN Al/Si constitutes for three T3 and three T4 sites (see Fig. 9), resulting in three Si in T3 sites changing NNN from Q^3(2Si,1Al) to one Q^3(3Si) and two Q^3(1Si,2Al), and three Si in T4 sites changing NNN from Q^3(1Si,2Al) to one Q^3(3Al) and two Q^3(2Si,1Al). The NNN of Si in all the T2 sites remain Q^4(3Si,1Al) and that of the Si exchanged into a T1 site is also Q^4(3Si,1Al). The NNN of Al in all the T1 sites remain Q^4(4Si), and that of the Al exchanged into a T2 site is also Q^4(4Si). Therefore, the NNN of Si and Al in Q^4 sites remain unchanged.

In the ordered structure, OH is in the T4(1Si,2Al)-OH···O-T3(2Si,1Al) configuration. The change in NNN environments of the six T3/T4 affects five OH sites that are each linked to one or two of these T3/T4 sites via O-H or H···O bond (see Fig. 9 and Table 6), resulting in the following altered configurations:

1: T4(1Si,2Al)-O···HO-T3(1Si,2Al) (for H252 in Table 6)

2: T4(1Si,2Al)-OH···O-T3(1Si,2Al) (for H245 in Table 6)

3: T4(2Si,1Al)-OH···O-T3(2Si,1Al) (for H241 in Table 6)

4: T4(2Si,1Al)-O···HO-T3(2Si,1Al) (for H250 in Table 6)

5: T4(3Al)-OH···O-T3(3Si) (for H249 in Table 6)

Thus, as a result of Si-Al disorder, 4 OH sites (1 to 4 above) now have T4/T3 on both sides having the same NNN (both (1Si,2Al) or both (2Si,1Al)), and the 5th OH has T4 and T3 on either side having NNN of 3Al and 3Si, respectively. These changes are accompanied by significant changes in hydrogen-bonding distances: much shorter for configurations 1 to 4, and longer for configuration 5 (see Table 6). Furthermore, for

411 configurations 1 and 4 above, H shifts position so that OH is bonded to T3 rather than T4
412 site in the relaxed structure.
413
414 **^{29}Si and ^{1}H NMR results.** The calculated ^{29}Si NMR results for disorder model 1 and
415 ordered structure are shown in Table 7 and Figure 10. The δ_i^{Si} has been referenced by
416 setting the peak for Q^3(2Si,1Al) in the ordered structure to the observed value of -87.94
417 ppm for the narrowest peak. The ordered structure produced three ^{29}Si NMR peaks for
418 Q^3(1Si,2Al), Q^3(2Si,1Al) and Q^4(3Si,1Al), which reasonably reproduced the observed main
419 peaks (within about 1 ppm), but cannot account for the additional peaks.
420 For the disorder model 1, the three main groups of ^{29}Si peaks now each contain a
421 distribution of δ_i^{Si}, including a smaller peak well shifted (by -2.1 and -1.3 ppm for
422 Q^3(1Si,2Al) and Q^3(2Si,1Al); -3.5 ppm for Q^4(3Si,1Al)) from the average position, which
423 may account for the observed multiple components and low-frequency tails in the ^{1}H-^{29}Si
424 CP spectra. Two additional peaks due to Q^3(3Al) and Q^3(3Si) are also produced, and are
425 respectively within 1.4 and 0.9 ppm of the observed two small peaks. All the main features
426 observed in the experimental NMR spectra are reproduced within about 1~3 ppm, which is
427 the typical uncertainty of such calculation.
428 In Figure 10 and supplementary Figure 6s, contributions from each of the four T sites
429 are also shown. As described above, the exchange of Si-Al over T1-O-T2 resulted in
430 changes of NNN for three T4 and three T3 sites. The latter are the origin for the two extra
431 peaks of Q^3(3Al) and Q^3(3Si) and the smaller peaks that contribute to low-frequency
432 extremes of the main peaks of Q^3(1Si,2Al) and Q^3(2Si,1Al). For Q^4, although all Si have

433 NNN of Q^4(3Si,1Al), the Si in T1 site has lower frequency than those in T2 sites, and may
434 account for the observed low-frequency tail.

435 The calculated ^{1}H NMR results for disorder model 1 and ordered structure are shown in
436 Table 6 and Figure 11. The ordered structure produces a single ^{1}H peak, which is used as a
437 reference for δ_i^H (13.85 ppm). For the disorder model 1, four OH sites with significantly
438 larger δ_i^H (15.6~16.1 ppm), and one with a smaller δ_i^H (11.7 ppm) are developed. They are
439 all within 0.6 ppm of the respective experimentally observed peaks. The remaining OH
440 sites give an average δ_i^H (13.7 ppm) close to that of the ordered structure, and show a
441 distribution from 13.3 to 13.9 ppm, with one OH site in particular displaced further to low
442 frequency. Thus, the observed features in the experimental ^{1}H NMR spectra are well
443 reproduced. The four OH sites that contribute to the 15~16 ppm peaks and one to the 11
444 ppm peak are, respectively, adjacent to one and two of the six T3/T4 sites that are NNN of
445 the Si-Al exchanged T1-(O)-T2 sites (also see Fig. 9).

446 Cross peaks in 2D ^{1}H-^{29}Si HETCOR spectra can also be predicted. In the relaxed
447 structure, each H is within 2.26~2.63 Å of the two Si(Q^3) in the Si-O-H···O-Si linkage, and
448 at > 4 Å to other Si. Therefore, within the spectral region for ^{29}Si Q^3, only correlation of ^{1}H
449 with the two nearest Si(Q^3) sites have significant contribution. From the configurations
450 described in the preceding section, the disorder model 1 predicts correlations that are the
451 same as observed in the 2D ^{1}H-^{29}Si HETCOR spectrum (see corresponding labels in Fig. 5a
452 and b). This allows the observed ^{29}Si NMR peaks to be assigned (see Table 7), assuming
453 the observed order in δ_i^{Si} for a given configuration is the same as that of the calculation.

454 Similarly, cross peaks in 2D ^{1}H DQ NMR spectrum can be predicted. In the relaxed
455 structure, each H is within 4.4~4.6 Å of two other H, and at > 7 Å from other H, so that

456 only the correlation with two nearest H sites need to be considered to account for the main
457 peaks. The simulated spectrum (Fig. 4b) shows that each of the five H sites in the 15~16
458 and 11 ppm region exhibit cross peaks only with the main peak, which again is consistent
459 with the observed spectrum. Among the peaks in the 15~16 ppm, the peak with the lowest
460 δ_i^H (labelled "4") is the only one that is correlated with the low-frequency shoulder (rather
461 than the peak maximum) of the main peak, again matching well with the observed spectrum.
462 Therefore, the 1D ^{29}Si (CP) MAS and ^{1}H MAS NMR spectra and 2D ^{1}H-^{29}Si HETCOR
463 and ^{1}H DQ MAS NMR spectra are all well reproduced by disorder model 1.
464 Although the calculation results for the other less plausible disorder models will not be
465 described in detail, it is worth mentioning model 2, as Si-Al disorder between T1 and T3
466 has been proposed by Ribbe (1974), and also used by Johnson and Rossman (2004) to
467 account for the observed ^{1}H NMR peak(s) in the 15~16 ppm region. For the latter, Johnson
468 and Rossman (2004) explained that the substitution of Si by Al in T3 site causes under-
469 bonding of O2(-Al) and thus increase in hydrogen-bonding strength. However, our first-
470 principles calculation for model 2 revealed that after structural relaxation, H shifted toward
471 Al to form Al-OH, yielding a ^{1}H chemical shift of 9.3 ppm, lower than that of the ordered
472 structure. Therefore, the energetically less favorable model of disorder over T1 and T3 not
473 only cannot explain the observed ^{29}Si NMR spectra, but also cannot account for the ^{1}H
474 NMR spectra.
475
476 **^{27}Al NMR results.** The calculated ^{27}Al NMR parameters for the ordered structure and
477 disorder model 1 of ussingite and low-albite are tabulated in Table 8. The calculated δ_i^{Al}
478 (60.1 ppm), C_Q^{Al} (3.7 MHz), η_Q^{Al} (0.89) and δ_1^{Al} (65.6 ppm) for the ordered ussingite are in

reasonable agreement (within 0.4 ppm, 0.7 MHz, 0.1, and 1.6 ppm, respectively) with those derived from the experimental data (see Table 4). The Al in T1 sites of the disorder model 1 yield average values close to those of the ordered structure, with a small distribution of values for each. The single Al in T2 site gave somewhat larger δ_i^{Al} (61.9 ppm) and δ_l^{Al} (67.0 ppm) values, and C_Q^{Al} (3.6 MHz) and η_Q^{Al} (0.74) within the range for Al in T1 sites. These results are broadly consistent with the experimental data that show moderate variation in NMR parameters and a small high-frequency tail in the isotropic projection of 2D 3QMAS NMR spectrum.

^{23}Na NMR results. The calculated ^{23}Na NMR parameters for the ordered structure and disorder model 1 of ussingite and low-albite are tabulated in Table 9. The calculated parameters for the two Na sites in the ordered ussingite are each close to the average values for disorder model 1. Both show similar C_Q^{Na} for the two Na sites, with Na1 yielding a larger η_Q^{Na} (close to 1) and smaller δ_i^{Na} than Na2. This supports the assignment of the peak with smaller δ_i^{Na} from the experimental data to Na1. The deviation in the calculated (average) values of δ_i^{Na}, C_Q^{Na} and η_Q^{Na} from the experimental NMR data are 2.5 ppm, 0.3~0.7 MHz and 0.2, respectively. The deviation in the difference of δ_i^{Na} between the two Na sites is smaller (0.0 ppm), which mimic trend for the calculated ^{23}Na chemical shielding in test calculations described earlier.

The individual parameters for each Na site in disorder model 1 show relatively large variations (especially in δ_i^{Na}, δ_l^{Na} and η_Q^{Na}): Na1: δ_i^{Na} of -3.2~3.8 ppm, C_Q^{Na} 2.1~3.4 MHz, η_Q^{Na} of 0.2~1.0 and δ_l^{Na} of 4.7~19.4 ppm; Na2: δ_i^{Na} of 0.2~7.3 ppm, C_Q^{Na} of 2.0~2.4 MHz, η_Q^{Na} of 0.3~0.9, and δ_l^{Na} of 8.9~16.9 ppm. The large, and partially overlapping ranges in

δ_i^{Na} and δ_l^{Na} for the two sites suggest that the two resolved peaks in the isotropic dimension of 2D 3QMAS NMR spectrum may each include contribution from the other Na site, although caution should be taken in interpreting the calculated δ_i^{Na} values. The large range in η_Q^{Na}, together with variations in other parameters, may account for the significant deviation from typical quadrupolar peak shape for a single site for the MAS projection of each peak in the 2D 3QMAS NMR spectrum. These results are, thus, broadly consistent with the experimental ^{23}Na NMR results and indicate local structural disorder around Na accompanying Si-Al disorder.

Discussions

Nature and extent of Si-Al disorder in ussingite

The 1D and 2D ^{29}Si and ^{1}H NMR results unambiguously revealed that there are more peaks from ussingite than are accountable by an ordered structure with ideal composition. In particular, the observation of ^{29}Si peaks attributable to Q^3(3Al) and Q^3(3Si), and the specific correlations for five smaller ^{1}H peaks in the 2D ^{1}H-^{29}Si HETCOR spectrum can be accounted for only by Si-Al disorder between T1 and T2 site, but not by Si-Al disorder between T1 and T3 site, as proposed previously, or by deviation in stoichiometry (excess Si or Al). The stoichiometric composition was also confirmed by EPMA analysis. Furthermore, the correlation of ^{29}Si peaks of Q^3(3Al) and Q^3(3Si) with a common ^{1}H peak suggests that Si-Al disorder occurs between neighboring T1-(O)-T2 site.

The first-principles calculation confirmed that Si-Al disorder over T1-O-T2 (disorder model 1) is energetically the most favorable, and also well reproduced all the observed

NMR features. It further revealed detailed spatial relationship: The Si-Al exchange over T1-O-T2 altered NNN environments of Si in three T3 and three T4 sites, which are the origin of the observed extra ^{29}Si peaks of Q^3(3Al) and Q^3(3Si), as well as the low-frequency shoulders/tails on the two main peaks of Q^3(1Si,2Al) and Q^3(2Si,1Al). The observed four extra ^{1}H peaks near 15~16 ppm and one near 11 ppm originate from five OH sites bonded or hydrogen-bonded to these six T3/T4 sites, contributing to the observed correlations in the 2D ^{1}H-^{29}Si HETCOR spectrum.

The extent of Si-Al disorder can be estimated from quantitative simulation results of ^{1}H and ^{29}Si NMR spectra described earlier. According to disorder model 1, exchange of one (out of 16) Al with Si over T1-O-T2 results in one Si of Q^3(3Al) and one of Q^3(3Si) (out of 32 Q^3 sites), and also four (out of 16) OH sites with δ_i^H of 15~16 ppm, and one near 11 ppm. Thus, the extent of Si-Al disorder, i.e., the proportion of Al in T1 site of the ordered structure that has exchanged with Si in T2 site, is expected to be equal to twice the proportion of Si of Q^3(3Al) or Q^3(3Si) among all Q^3 sites, and also equal to the proportion of protons (among all protons) that contribute to the peak near 11 ppm, and also equal to 1/4 of the proportion of all protons that contribute to peaks in the 15~16 ppm range in ^{1}H MAS NMR spectra. From ^{29}Si NMR, the extent of Si-Al disorder was obtained separately from the relative intensity (among Q^3) of the peak of Q^3(3Al) and that of Q^3(3Si) in the ^{1}H-^{29}Si CP MAS NMR spectra with long contact times (12 and 20 ms) (see Table 2). The somewhat larger relative intensity for Q^3(3Al) than Q^3(3Si) is most likely due to somewhat faster CP rate, as a result of shorter Si-H distance, for the former. The average of the two values is expected to be less susceptible to such effect. The result is 3.4(0.8)% and 3.3(0.9)% Si-Al disorder for sample 1 and 2, respectively (see Table 2). From ^{1}H NMR, it

This is the peer-reviewed, final accepted version for American Mineralogist, published by the Mineralogical Society of America.
The published version is subject to change. Cite as Authors (Year) Title. American Mineralogist, in press.
DOI: https://doi.org/10.2138/am-2023-9008. http://www.minsocam.org/

548 was estimated separately from the sum of relative intensities for peaks in the 15~16 ppm
549 range and from that near 11 ppm. The result is 2.7(0.4)% and 2.8(0.6)% Si-Al disorder for
550 sample 1 and 2, respectively (see Table 3). Thus, both the ^{29}Si and ^{1}H NMR data yielded
551 consistent estimation of the extent of Si-Al disorder of ~3% for both samples.
552 For comparison, we also made similar estimation using the ^{1}H NMR result reported by
553 Johnson & Rossman (2004) for ussingite from IIimaussaq, Greenland. The result is 2% Si-
554 Al disorder (see Table 3), which is 1/4 of their inference, but close to those from the present
555 study.
556 The extent of Si-Al disorder is expected to be temperature dependent. The similar values
557 derived for ussingite from two different localities may indicate similar hydrothermal
558 temperature conditions in their genesis.
559
560 **Correlation between Si-Al disorder and hydrogen-bonding distance variations**
561 The combined NMR experiment and first-principles calculation allowed us to reveal a
562 clear picture for the correlation between Si-Al disorder and hydrogen-bonding distance
563 variation.
564 In Figure 12, the O-H and H···O distances, Si-O(-H) and Si-O(···H) distances, and δ_i^H
565 are plotted against O···O distance for the Si-O-H···O-Si linkage. Good correlation is
566 observed among the hydrogen-bonding distances and δ_i^H, with stronger hydrogen bonding
567 yielding shorter H···O and O···O distances, longer O-H distance, and larger δ_i^H. Such a
568 correlation is well known for inorganic and organic compounds (c.f., Johnson and Rossman,
569 2004; Xue and Kanzaki, 2009). More intriguing is that the Si-O(H) and Si-O(···H) bond
570 distances on either side of the hydrogen bond also exhibit systematic changes that are

571 correlated with changes in the hydrogen-bonding distances. There is a clear pattern of
572 alternating increase and decrease in bond distance along the Si-O-H···O-Si linkage. Similar
573 observation of alternating changes in bond distance along a general hydrogen-bonding
574 system X–D–H···A–Y (D: hydrogen bond donor; A: hydrogen bond acceptor) has been
575 reported previously (e.g., Mohri, 2006) and may be a representative feature of strong
576 hydrogen bonding.

577 The origin of the variation in hydrogen-bonding and Si-O(-H, ···H) distances may be
578 traced to variation in the NNN environments of the two Si sites on either end of the
579 hydrogen bond as a result of Si-Al disorder over T1-O-T2. This is clear from the correlation
580 between Si-O(-H, ···H) distances and the difference in the number of NNN Al between the
581 two Si sites, with smaller contrast tends to bring the two distances closer to each other (Fig.
582 12d).

583 These observations can be well accounted for by the bond valence model, which
584 requires the sum of bond valences around any ion to be equal to the valence of the ion
585 (valence sum rule) to ensure local charge neutrality, with the bond valence being a function
586 of bond distance (e.g., $S_{ij} = \exp((R_0-R_{ij})/B$, where S_{ij} and R_{ij} are the bond valence and bond
587 distance between atom i and j, and R_0 and B are constant parameters) (cf. Brown, 2002).
588 The effect of changes in NNN environments of Si (as a result of Si-Al disorder over T1-O-
589 T2) on the hydrogen-bonding distances has, thus, been transmitted via bond valence
590 (distance) changes along the bonding network, in such a way so that all the bond distances
591 along the Si-O-H···O-Si linkage are inter-correlated. The fact that OH is bonded to
592 T4(1Si,2Al), rather than T3(2Si,1Al) in the ordered structure can also be understood from
593 bond valence consideration.

This is the peer-reviewed, final accepted version for American Mineralogist, published by the Mineralogical Society of America.
The published version is subject to change. Cite as Authors (Year) Title. American Mineralogist, in press.
DOI: https://doi.org/10.2138/am-2023-9008. http://www.minsocam.org/

Implications

The complete clarification of the nature and extent of Si-Al disorder in ussingite, which could not be unambiguously determined so far despite X-ray diffraction (Rossi et al., 1974), neutron diffraction (Williams and Weller, 2012), and ^{29}Si (Oglesby and Stebbins, 2000) and ^{1}H NMR studies (Johnson and Rossman, 2004), is in itself of significance in understanding the crystal chemistry of ussingite, a mineral with an unique interrupted framework structure. Moreover, the insights gained have implications far beyond that as outlined below.

Effect of Si-Al disorder on hydrogen-bonding variations in general. Particularly impressive are the findings of this study on the extent to which Si-Al disorder can bring about on the variation in hydrogen-bonding distance, and the crystal chemical insights gained into the correlation between NNN environments of Si and hydrogen-bonding distance variation. This is most likely a general phenomenon also applicable to other hydrous minerals.

Many hydrous aluminosilicate minerals, including important mantle minerals, such as topaz-OH (Xue et al., 2010), phase egg (Xue et al., 2006), aluminous phase E, phase C (=superhydrous phase B and phase D (Pamato et al., 2015) show Si-Al disorder. Much attention has been paid to the hydrogen-bonding behavior of these hydrous minerals, as it may have a significance influence on various physical properties. However, the effect of Si-Al disorder on the hydrogen-bonding distance have been largely overlooked. A systematic investigation over a wide range of hydrous aluminosilicate minerals is warranted.

Si/Al partitioning tendency in partially depolymerized aluminosilicate system. The partition behavior of Al/Si over different Q^n species, especially between Q^4 and more depolymerized Q^n species is an issue of great interest in understanding the structure and properties of aluminosilicate melts/glasses. The confirmation that the Si-Al disorder in ussingite in fact occurs over T1-O-T2 that avoids the formation of Al-O-Al and Al(Q^3) is consistent with trend observed so far for partially depolymerized anhydrous and hydrous aluminosilicate glasses (e.g., Allwardt et al., 2003; Neuville et al., 2004; Xue and Kanzaki, 2008), and provided crystal chemical insight into such trend.

Nature and hydrogen-bonding strength of OH in (alumino)silicate system. Johnson and Rossman (2004) and Williams and Weller (2012) both mentioned interest in using ussingite as a model for OH defects in nominally anhydrous albite (and other plagioclase feldspar minerals). However, the two minerals turned out to have very different OH environments: whereas ussingite exhibits strong hydrogen bonding, that in albite is much weaker (δ_i^H 4~6 ppm) (Johnson and Rossman, 2004). This "negative" result carries an important, though often neglected implication, i.e., the key role of (de)polymerization, or the presence/absence of network modifying cations (other than H). Whereas albite is fully polymerized, ussingite is partially depolymerized with NBO/T (0.5) in the range for natural andesitic magma. SiOH groups in alkali and alkaline earth silicate glasses have been found to have stronger hydrogen bonding and thus larger δ_i^H (4~17 ppm) than that of silica glasses (δ_i^H ~3 ppm), and the fraction with stronger hydrogen bonding (larger δ_i^H) increases with decreasing field strength of the network modifying cation (from Ca/Mg to Li to Na),

640 which has been interpreted as enhanced hydrogen bonding by NBO as hydrogen-bond
641 acceptor (Xue and Kanzaki, 2004). The observation of much stronger hydrogen bonding in
642 ussingite than in albite is consistent with, and provides crystal chemical insight into such
643 observation. Other hydrous silicate minerals with strong hydrogen bonding, such as
644 pectolite ($NaCa_2Si_3O_8OH$) and serandite ($NaMn_2Si_3O_8OH$), also have depolymerized
645 structure containing network-modifying cations of low field strength (Na). Ussingite, as an
646 aluminosilicate mineral, is also valuable in revealing the preferential formation of SiOH
647 over $Al^{IV}OH$. It is worth mentioning for completeness that for depolymerized minerals
648 containing network modifying cations of higher field strength (e.g., Ca, Mg, Al^{VI}), such as
649 amphibole, humite group minerals and prehnite, OH tends to bond only to network
650 modifying cations, forming MOH (free OH) groups that often have weak hydrogen bonding.
651 The presence of free OH in depolymerized Ca-Mg (alumino)silicate glasses has also been
652 reported (e.g., Xue and Kanzaki, 2004; Xue and Kanzaki, 2009). Therefore, the
653 presence/absence of network-modifying cations and its field strength are important factors
654 controlling the nature and hydrogen bonding strength of OH in both minerals and glasses.
655 With that criterion, ussingite is not a good model for albite and other fully polymerized
656 minerals, but a valuable model for partially depolymerized aluminosilicate minerals and
657 glasses/melts containing network modifying cations of low field strength.
658
659 **Importance of local structural relaxation around disorder/defect sites**. It is not rare
660 to encounter publications that attempted to infer the location of defects based on geometry
661 of the ordered structure, but were subsequently proved to be wrong, because structural

662 relaxation around defects may significantly alter the local geometry (cf. Xue et al., 2017 for
663 a review of an example for olivine).

664 This study represents another case study. It was revealed that for Al-Si exchange over
665 T1-O-T2 of ussingite, the hydrogen bonding O8···O2 distance in the T4-O8-H···O2-T3
666 linkage can vary by ~0.1 Å (δ_i^H by ~5 ppm) depending on the NNN of T3/T4 sites.
667 Furthermore, for some configurations, H shifts toward T3 so that O2 becomes the hydrogen
668 bond doner. Such variations would be difficult to identify using diffraction techniques, but
669 should be important in understanding its physical properties. Also, as mentioned above,
670 Johnson and Rossman (2004) used Si-Al disorder between T1 and T3 to account for the
671 observed ^{1}H NMR peak(s) with larger δ_i^H. However, our calculation revealed that the
672 resultant δ_i^H is smaller than that of the ordered structure due to shift of H position toward
673 Al accompanying structural relaxation. First-principles calculation is particularly helpful in
674 revealing the locally relaxed structure.

675 Finally, this study has demonstrated that the combined comprehensive 1D and 2D multi-
676 nuclear NMR measurements and first-principles calculation is effective in revealing
677 detailed spatial relationship around disorder in minerals, which would be difficult to gain
678 from any other single technique.

679

680 **Acknowledgements**

681 We thank two anonymous reviewers for constructive comments, and Tsutomu Ota for
682 assistance with EPMA analysis. The purchase of the Bruker Avance NEO NMR
683 spectrometer, which made this study possible, was supported by JSPS grant (Kiban-A, No.
684 17H01174 to XX) and operational expenses grant from Okayama University.

685

686 **References Cited**

687 Allwardt, J.R., Lee, S.K., and Stebbins, J.F. (2003) Bonding preferences of non-bridging O
688 atoms: Evidence from ^{17}O MAS and 3QMAS NMR on calcium aluminate and low-
689 silica Ca-aluminosilicate glasses. American Mineralogist, 88(7), 949-954.
690 Amoureux, J.-P., and Fernandez, C. (1998) Triple, quintuple and higher order multiple
691 quantum MAS NMR of quadrupolar nuclei Solid State Nuclear Magnetic Resonance,
692 10(4), 211-223.
693 Amoureux, J.P., Delevoye, L., Steuernagel, S., Gan, Z., Ganapathy, S., and Montagne, L.
694 (2005) Increasing the sensitivity of 2D high-resolution NMR methods applied to
695 quadrupolar nuclei. Journal of Magnetic Resonance, 172(2), 268-278.
696 Anthony, J.W., Bideaux, R.A., Bladh, K.W., and Nichols, M.C. Handbook of Mineralogy.
697 Mineralogical Society of America, Chantilly, VA 20151-1110, USA,
698 http://www.handbookofmineralogy.org/.
699 Brown, I.D. (2002) The chemical bond in inorganic chemistry: The Bond valence model.
700 278 p. Oxford Science Publications.
701 Dal Corso, A. (2014) Pseudopotentials periodic table: From H to Pu. Computational
702 Materials Science, 95, 337-350.
703 Gan, Z.H., and Kwak, H.T. (2004) Enhancing MQMAS sensitivity using signals from
704 multiple coherence transfer pathways. Journal of Magnetic Resonance, 168(2), 346-
705 351.
706 Giannozzi, P., Andreussi, O., Brumme, T., Bunau, O., Nardelli, M.B., Calandra, M., Car,
707 R., Cavazzoni, C., Ceresoli, D., Cococcioni, M., Colonna, N., Carnimeo, I., Dal
708 Corso, A., de Gironcoli, S., Delugas, P., DiStasio, R.A., Ferretti, A., Floris, A.,
709 Fratesi, G., Fugallo, G., Gebauer, R., Gerstmann, U., Giustino, F., Gorni, T., Jia, J.,
710 Kawamura, M., Ko, H.Y., Kokalj, A., Kucukbenli, E., Lazzeri, M., Marsili, M.,
711 Marzari, N., Mauri, F., Nguyen, N.L., Nguyen, H.V., Otero-de-la-Roza, A., Paulatto,
712 L., Ponce, S., Rocca, D., Sabatini, R., Santra, B., Schlipf, M., Seitsonen, A.P.,
713 Smogunov, A., Timrov, I., Thonhauser, T., Umari, P., Vast, N., Wu, X., and Baroni,
714 S. (2017) Advanced capabilities for materials modelling with QUANTUM
715 ESPRESSO. Journal of Physics-Condensed Matter, 29(46).
716 Giannozzi, P., Baroni, S., Bonini, N., Calandra, M., Car, R., Cavazzoni, C., Ceresoli, D.,
717 Chiarotti, G.L., Cococcioni, M., Dabo, I., Corso, A.D., Gironcoli, S.d., Fabris, S.,
718 Fratesi, G., Gebauer, R., Gerstmann, U., Gougoussis, C., Kokalj, A., Lazzeri, M.,
719 Martin-Samos, L., Marzari, N., Mauri, F., Mazzarello, R., Paolini, S., Pasquarello, A.,

Paulatto, L., Sbraccia, C., Scandolo, S., Sclauzero, G., Seitsonen, A.P., Smogunov, A., Umari, P., and Wentzcovitch, R.M. (2009) QUANTUM ESPRESSO: a modular and open-source software project for quantum simulations of materials. Journal of Physics: Condensed Matter, 21(39), 395502.

Hohwy, M., Jakobsen, H.J., Eden, M., Levitt, M.H., and Nielsen, N.C. (1998) Broadband dipolar recoupling in the nuclear magnetic resonance of rotating solids: A compensated C7 pulse sequence. Journal of Chemical Physics, 108(7), 2686-2694.

Ishii, Y., and Tycko, R. (2000) Sensitivity enhancement in solid state ^{15}N NMR by indirect detection with high-speed magic angle spinning. Journal of Magnetic Resonance, 142(1), 199-204.

Johnson, E.A., and Rossman, G.R. (2004) An infrared and ^{1}H MAS NMR investigation of strong hydrogen bonding in ussingite, $Na_2AlSi_3O_8(OH)$. Physics and Chemistry of Minerals, 31(2), 115-121.

Kanzaki, M., and Xue, X. (2016) Cation distribution in Mg-Zn olivine solid solution: a ^{29}Si MAS NMR and first-principles calculation study. Journal of Mineralogical and Petrological Sciences, 111, 292-296.

Kirkpatrick, R.J. (1988) MAS NMR spectroscopy of minerals and glasses. In F.C. Hawthorne, Ed. Spectroscopic Methods in Mineralogy and Geology, 18, p. 341-403. Mineralogical Society of America, Washington, D.C.

Lowenstein, W. (1954) The distribution of aluminum in the tetrahedra of silicates and aluminates. American Mineralogist, 39, 92-96.

Mohri, F. (2006) A molecular orbital explanation of bond distance variation caused by hydrogen bond formation. Journal of Molecular Structure-Theochem, 770(1-3), 179-184.

Momma, K., and Izumi, F. (2011) VESTA 3 for three-dimensional visualization of crystal, volumetric and morphology data. Journal of Applied Crystallography, 44, 1272–1276.

Neuville, D.R., Cormier, L., and Massiot, D. (2004) Al environment in tectosilicate and peraluminous glasses: A ^{27}Al MQ-MAS NMR, Raman, and XANES investigation. Geochimica et Cosmochimica Acta, 68(24), 5071-5079.

Oglesby, J.V., and Stebbins, J.F. (2000) ^{29}Si CPMAS NMR investigations of silanol-group minerals and hydrous aluminosilicate glasses. American Mineralogist, 85, 722-731.

Pamato, M.G., Myhill, R., Ballaran, T.B., Frost, D.J., Heidelbach, F., and Miyajima, N. (2015) Lower-mantle water reservoir implied by the extreme stability of a hydrous aluminosilicate. Nature Geoscience, 8(1), 75-79.

Perdew, J.P., Burke, K., and Ernzerhof, M. (1996) Generalized gradient approximation made simple. Physical Review Letters, 77(18), 3865-3868.

Perdew, J.P., Ruzsinszky, A., Csonka, G.I., Vydrov, O.A., Scuseria, G.E., Constantin, L.A., Zhou, X., and Burke, K. (2008) Restoring the Density-Gradient Expansion for Exchange in Solids and Surfaces. Physical Review Letters, 100(13), 136406.

Pickard, C.J., and Mauri, F. (2001) All-electron magnetic response with pseudopotentials: NMR chemical shifts. Physical Review B, 63(24), 245101.

Ribbe, P.H. (1974) A comparison of bonding effects in ussingite and low albite. American Mineralogist, 59, 341-344.

Rossi, G., Tazzoli, V., and Ungaretti, L. (1974) The crystal structure of ussingite. American Mineralogist, 59, 335-340.

Sanchez-Munoz, L., Florian, P., Gan, Z.H., and Munoz, F. (2022) Order-Disorder Diversity of the Solid State by NMR: The Role of Electrical Charges. Minerals, 12(11).

Smith, J.V., Artioli, G., and Kvick, Å. (1986) Low albite, $NaAlSi_3O_8$: Neutron diffraction study of crystal structure at 13 K. American Mineralogist, 71, 727-733.

Stebbins, J.F. (1992) Nuclear Magnetic Resonance Spectroscopy of Geological Materials. MRS Bulletin, 17(5), 45-52.

Stebbins, J.F., and Xue, X. (2014) NMR spectroscopy of inorganic Earth materials. In F.C. Hawthorne, Ed. Spectroscopic Methods in Mineralogy and Geology, 78, p. 605-653. Mineralogical Society of America, Washington, D.C.

Thakur, R.S., Kurur, N.D., and Madhu, P.K. (2008) An analysis of phase-modulated heteronuclear dipolar decoupling sequences in solid-state nuclear magnetic resonance. Journal of Magnetic Resonance, 193(1), 77-88.

Williams, E.R., and Weller, M.T. (2012) A variable-temperature neutron diffraction study of ussingite; a strong asymmetric hydrogen bond in an aluminosilicate framework. Physics and Chemistry of Minerals, 39(6), 471-478.

Xue, X., and Kanzaki, M. (2004) Dissolution mechanisms of water in depolymerized silicate melts: Constraints from ^{1}H and ^{29}Si NMR spectroscopy and ab initio calculations. Geochimica et Cosmochimica Acta, 68(24), 5027-5057.

-. (2008) Structure of hydrous aluminosilicate glasses along the diopside - anorthite join: a comprehensive one- and two- dimensional ^{1}H and ^{27}Al NMR study Geochimica et Cosmochimica Acta, 72(9), 2331-2348.

Xue, X., and Kanzaki, M. (2009) Proton distributions and hydrogen bonding in crystalline and glassy hydrous silicates and related inorganic materials: insights from high-resolution solid-state NMR spectroscopy. Journal of the American Ceramic Society, 92(12), 2803-2830.

790 Xue, X., Kanzaki, M., and Fukui, H. (2010) Unique crystal chemistry of two polymorphs of
791 topaz-OH: a multi-nuclear NMR and Raman study. American Mineralogist, 95, 1276-
792 1293.
793 Xue, X., Kanzaki, M., Fukui, H., Ito, E., and Hashimoto, T. (2006) Cation order and
794 hydrogen bonding of high-pressure phases in the Al_2O_3-SiO_2-H_2O system: An NMR
795 and Raman study. American Mineralogist, 91, 850-861.
796 Xue, X., Kanzaki, M., Turner, D., and Loroch, D. (2017) Hydrogen incorporation
797 mechanisms in forsterite: New insights from ^{1}H and ^{29}Si NMR spectroscopy and first-
798 principles calculation. American Mineralogist, 102(3), 519-536.
799 Xue, X., and Stebbins, J.F. (1993) ^{23}Na NMR chemical shifts and local Na coordination
800 environments in silicate crystals, melts and glasses. Physics and Chemistry of
801 Minerals, 20, 297-307.
802

803

804 **Figure captions**

805 Figure 1. Crystal structure of ussingite from neutron diffraction (Williams and Weller,
806 2012). Blue and grey tetrahedra represent SiO_4 and AlO_4 tetrahedra, respectively. Red
807 and pink spheres represent oxygen and hydrogen atoms, respectively. The black box
808 delineates the unit cell dimension. The four crystallographycally unique T sites, two Na
809 sites, and the O8-H···O2 hydrogen bond are also shown. Drawn using the Vesta
810 program (Momma and Izumi, 2011).

811 Figure 2. ^{29}Si MAS NMR spectrum of ussingite sample 1 at a spinning rate of 20 kHz, (a)
812 and ^{1}H-^{29}Si CP MAS NMR spectra at a spinning rate of 10 kHz and contact time of 20
813 ms for sample 1 (b) and sample (2)(c).

814 Figure 3. ^{1}H MAS NMR spectra at a spinning rate of 24 kHz for ussingite sample 1 (a) and
815 2 (b).

816 Figure 4. 2D rotor-synchronized ^{1}H DQ MAS NMR spectrum for ussingite sample 1 at a
817 spinning rate of 14.7 kHz using the POST-C7 scheme with total projections shown for
818 both dimensions **(a)**, and schematic 2D ^{1}H DQ MAS NMR spectrum predicted from
819 first-principles calculation for ussingite disorder model 1 **(b)**. For (b), the projection at
820 the top is the 1D spectrum shown in Fig. 11b, and cross peak positions in the 2D area
821 are simply shown as circles for ^{1}H-^{1}H pairs within 4 Å. The red line in both is a guide

for diagonal peaks. The labels 1 to 5 in both correspond to H in the five configurations affected by Si-Al disorder described in the text.

Figure 5. 2D ^{1}H-^{29}Si HETCOR spectrum for ussingite sample 1 using the ^{1}H→^{29}Si→^{1}H double CP scheme at a spinning rate of 24 kHz and a contact time of 8 ms with total projections shown for both dimensions **(a)**, and schematic 2D ^{1}H-^{29}Si HETCOR spectrum predicted from first-principles calculation for ussingite disorder model 1 **(b)**. For (b), projections in the two dimensions are the 1D spectra shown in Fig. 10b and 11b, and cross peak positions in the 2D area are simply shown as circles for ^{1}H-^{29}Si pairs in the Si-OH···O-Si linkage. The labels 1 to 5 in both correspond to the five configurations affected by Si-Al disorder described in the text.

Figure 6. ^{27}Al MAS NMR spectra (**a**: full range with intensity truncated for the central band, **c**: central band) for ussingite sample 1 at a spinning rate of 20 kHz, and the respective simulated spectra using parameters in Table 4 **(b, d)**.

Figure 7. 2D rotor-synchronized ^{27}Al SPAM-3QMAS NMR spectrum of ussingite sample 1 at a spinning rate of 20 kHz with total projections shown for both dimensions.

Figure 8. 2D rotor-synchronized ^{23}Na SPAM-3QMAS NMR spectrum of ussingite sample 1 at a spinning rate of 20 kHz with total projections shown for both dimensions **(a)**, and 1D ^{23}Na MAS NMR spectra for ussingite sample 1 at a spinning rate of 20 kHz, its

840 simulated spectrum, sum of F_2 cross sections (F_1 range: 7.0~12.5 ppm for peak 1;
841 12.5~18.0 ppm for peak 2) for each of the two peaks labelled in (a) and the respective
842 simulated spectrum as labelled **(b)**. All simulations used parameters in Table 4.

843 Figure 9. Local structure around the Al-Si exchanged T1-O-T2 linkage for ussingite
844 disorder model 1. For clarity, whereas SiO_4 and AlO_4 tetrahedra for T1 and T2 are
845 shown as blue and grey tetrahedra as in Figure 1, the SiO_4 tetrahedra for their NNN T4
846 sites are shown in brown, and those for T3 sites are shown in purple. The five H sites
847 that are bonded or hydrogen-bonded to these T3 and T4 sites are shown as black circles.
848 The H sites are labeled as in Figures 4b and 5b. Drawn using the Vesta program
849 (Momma and Izumi, 2011).

850 Figure 10. ^{1}H-^{29}Si CP MAS NMR spectrum for ussingite sample 1 (same as Fig. 2b) **(a)**,
851 and predicted ^{29}Si spectra for disorder model 1 **(b)** and ordered structure **(c)** of
852 ussingite from first-principles calculation. For the latter two, an arbitrary Lorentzian
853 line broadening of 20 Hz was applied.

854 Figure 11. ^{1}H MAS NMR spectrum for ussingite sample 1 (same as Fig. 3a) **(a)**, and
855 predicted spectra for disorder model 1 **(b)** and ordered structure **(c)** of ussingite from
856 first-principles calculation. For the latter two, an arbitrary Lorentzian line broadening
857 of 20 Hz was applied.

858 Figure 12. Plot of O-H and H···O distances **(a)**, ^{1}H isotropic chemical shift (δ_i^H) **(b)**, and
859 Si-O(-H) and Si-O(···H) distances **(c)** as a function of O···O distance, and Si-O(-H)
860 and Si-O(···H) distances as a function of the difference in the number of Al in the
861 NNN of the two Si (Q^3) sites **(d)** for Si-O-H···O-Si linkages in disorder model 1 and
862 ordered structure of ussingite from first-principles calculation as labeled.
863

Table 1. Electron microprobe analysis result for ussingite

Sample	Sample 1	Sample 2
Oxides (wt%)		
SiO_2	59.23(0.50)	58.92(0.32)
Al_2O_3	16.30(0.21)	16.38(0.20)
CaO	0.03(0.03)	0.02(0.03)
Na_2O	20.29(0.47)	20.79(0.33)
K_2O	0.05(0.05)	0.02(0.02)
Total	95.91(0.40)	96.14(0.50)
Cations per 8.5 O atoms for anhydrous components		
Si	3.01(0.01)	3.00(0.01)
Al	0.98(0.01)	0.98(0.01)
Ca	0.00(0.00)	0.00(0.00)
Na	2.00(0.05)	2.05(0.03)
K	0.00(0.00)	0.00(0.00)
Total	6.00(0.04)	6.04(0.02)

Note: 9 points were averaged for each sample with the standard deviation reported in brackets.

This is the peer-reviewed, final accepted version for American Mineralogist, published by the Mineralogical Society of America.
The published version is subject to change. Cite as Authors (Year) Title. American Mineralogist, in press.
DOI: https://doi.org/10.2138/am-2023-9008. http://www.minsocam.org/

867 Table 2. Relative peak intensities among Q^3 and extent of Si-Al disorder in ussingite from ^{1}H-^{29}Si CP MAS NMR

Sample	Contact time (ms)	Relative intensity (%)				Extent of Si-Al disorder (%)			
		Q^3(3Al) (-81 ppm)	Q^3(1Si,2Al) (-83~-86 ppm)	Q^3(2Si,1Al) (-88~-89 ppm)	Q^3(3Si) (-91.6 ppm)	Method 1[a]	Method 2[a]	Average	Standard deviation
Sample 1	20	2.08	49.08	47.53	1.31	4.15	2.62	3.4	0.8
	12	1.97	49.67	47.01	1.35	3.94	2.70		
Sample 2	20	1.87	48.76	48.04	1.33	3.75	2.65	3.3	0.9
	12	2.22	49.62	46.89	1.27	4.45	2.53		

Notes: Each group of peaks includes one (-81 ppm), seven (-83~-86 ppm), three (-88~-89 ppm) and one (-91.6 ppm) component(s). Extent of Si-Al disorder refers to the proportion of Al in T1 site (of the ordered structure) that has exchanged with Si in T2 site.

[a] Method 1: Estimated to be equal to twice the relative intensity (among all Q^3) of peak due to Q^3(3Al); Method 2: Estimated to be equal to twice the relative intensity of peak due to Q^3(3Si)(see text for explanation).

868

869 Table 3. Relative intensities and extent of Si-Al disorder in ussingite from ^{1}H MAS NMR

Sample	Spinning rate (kHz)	Relative intensity (%)			Extent of Si-Al disorder (%)			
		15~16 ppm	13~14 ppm	11 ppm	Method 1[a]	Method 2[a]	Average	Standard deviation
Sample 1	24	9.57	87.55	2.89	2.39	2.89	2.7	0.4
	20	9.64	87.15	3.21	2.41	3.21		
Sample 2	24	8.72	88.00	3.27	2.18	3.27	2.8	0.6
	20	9.27	87.38	3.35	2.32	3.35		
J&R[b]	6 &12	8	90	2	2	2	2	0

Notes: Each group of peak includes four (15~16 ppm), two (13~14 ppm) and one (11 ppm) component(s). Extent of Si-Al disorder refers to the proportion of Al in T1 site (of the ordered structure) that has exchanged with Si in T2 site.

[a] Method 1: Estimated to be 1/4 of the total relative intensity of peaks in the 15~16 ppm range (among all peaks); Method 2: Estimated to be equal to the relative intensity of the 11-ppm peak.

[b] Reported by Johnson & Rossman (2004) for a sample from IIimaussaq, Greenland.

870

871

872

873 Table 4. ^{27}Al and ^{23}Na NMR parameters of ussingite from simulation of MAS NMR spectra

Site	δ_i (ppm)	C_Q (MHz)	η_Q	δ_1 (ppm)[a]	δ_1 obs (ppm)[a]
Al	60.45(0.2)	3.02(0.04)	0.82(0.04)	64.1	64.0
Na1	-2.9(0.2)	2.69(0.04)	1.00(0.02)	9.8	9.8
Na2	2.1(0.2)	3.02(0.04)	0.41(0.04)	14.7	14.7

Note: Because of the distribution of parameters for both ^{27}Al and ^{23}Na, the estimated values should be regarded as a rough average value.

[a] δ_1 and δ_1 obs are the peak position expected from the estimated parameters, and the peak maximum position actually observed, in the isotropic (F_1) dimension of 3QMAS NMR spectra, with $\delta_1 = \delta_i - \frac{10}{17}\delta_Q$, and $\delta_Q = -10^5 \times \frac{3(4I(I+1)-3)}{(4I(2I-1))^2} \times \left(\frac{C_Q}{\nu_Q}\right)^2 \times \left(1 + \frac{\eta_Q{}^2}{3}\right)$, where I is the spin quantum number (5/2 for ^{27}Al, 3/2 for ^{23}Na), and ν_0 is the resonance frequency (104.27 MHz for ^{27}Al, 105.84 MHz ^{23}Na).

874 Table 5. Enthalpy difference (ΔE) and volume (V) at 1 bar for different ussingite models

Model	Si-Al exchange	ΔE(kJ/mol)	ΔE(kJ/mol)	V(A^3)
Ordered	none	0		3204.47
Disorder model 1	T1-(O)-T2	28.44	0	3208.09
Disorder model 2	T1-(O)-T3	56.72	28.28	3206.28
Disorder model 3	T1-(O)-T4	80.46	52.01	3207.56
Disorder model 4	T1-(O)-T4	83.05	54.61	3207.40
Disorder model 5	remote T1-T2 pair	96.97	68.52	3208.24
Experiment (XRD, ambient condition)[a]				3195.44
Experiment (ND, 4 K)[b]				3170.36

Note: all values refer to that of 2 × 2 × 2 supercell.
[a] from Rossi et al. (1974).
[b] Neutron diffraction (ND) from Williams & Weller (2012).

875

This is the peer-reviewed, final accepted version for American Mineralogist, published by the Mineralogical Society of America.
The published version is subject to change. Cite as Authors (Year) Title. American Mineralogist, in press.
DOI: https://doi.org/10.2138/am-2023-9008. http://www.minsocam.org/

876 Table 6. ^{1}H chemical shift and bond distances and angles in the Si-O-H···O-Si linkage of ussingite from first-principles calculation

H site no.[a]	σ_i^H (ppm)[b]	δ_i^H (ppm)[b]	Sin1-On1-Hn···On2-Sin2	Sin1(NNN)[d]	Sin2(NNN)[d]	R(Sin1-On1)(A)	R(On1-Hn)(A)	R(On2-Hn)(A)	R(On1···On2)(A)	R(On2-Sin2)(A)	∠On1-Hn-On2(°)	δ_i^H,exp (ppm)
Ordered structure												
	14.89	13.85	Si11-O27-H31···O15-Si9	T4(1Si,2Al)	T3(2Si,1Al)	1.636	1.094	1.374	2.467	1.598	177.167	13.85
Disorder model 1												
241(3)	12.96	15.78	Si81-O209-H241···O121-Si73	**T4(2Si,1Al)**	T3(2Si,1Al)	1.617	1.164	1.264	2.428	1.606	177.124	15.54
245(2)	12.77	15.97	Si85-O213-H245···O125-Si77	T4(1Si,2Al)	**T3(1Si,2Al)**	1.623	1.190	1.233	2.422	1.617	177.755	15.47
249(5)	17.03	11.71	Si89-O217-H249···O113-Si65	**T4(3Al)**	**T3(3Si)**	1.654	1.057	1.455	2.511	1.584	175.919	11.1
250(4)	13.10	15.64	Si66-O114-H250···O218-Si90[c]	T3(2Si,1Al)	**T4(2Si,1Al)**	1.620	1.160	1.279	2.438	1.610	178.126	15.1
252(1)	12.63	16.11	Si68-O116-H252···O220-Si92[c]	**T3(1Si,2Al)**	T4(1Si,2Al)	1.618	1.204	1.210	2.414	1.617	178.131	15.8
11 other H sites (with NNN of Si on both ends unaffected by Si-Al disorder):												
mean	14.99	13.75	Sin1-On1-Hn···On2-Sin2	T4(1Si,2Al)	T3(2Si,1Al)	1.636	1.091	1.379	2.469	1.598	177.180	13.85
maximum	15.40	13.98		T4(1Si,2Al)	T3(2Si,1Al)	1.637	1.095	1.397	2.478	1.600	177.546	
minimum	14.76	13.34		T4(1Si,2Al)	T3(2Si,1Al)	1.634	1.082	1.367	2.462	1.596	176.995	

[a] Numbers in brackets correspond to configuration numbers labelled in Figures 4b, 5b and 6, and described in the text.
[b] σ_i^H: ^{1}H isotropic shielding; δ_i^H: ^{1}H isotropic chemical shift referenced to the experimental value (13.85 ppm) for the strongest peak of ussingite, i.e., $\delta_i^H = 13.85+14.89-\sigma_i^H$.
[c] The O-H bond has shifted from T4 to T3 side for H250 and H252.
[d] Bold letters highlight T3 and T4 sites whose NNN are different from that of the ordered structure.

877

878 Table 7. ^{29}Si chemical shift from first-principles calculation

T site	Si site no.	σ_i^{Si} (ppm)[a]	δ_i^{Si},calc (ppm) [a]	δ_i^{Si},exp (ppm) [b]	NNN[c]
			Low-albite		
T1m		455.35	-107.75	-104.5	Q4(3Si,1Al)
T2o		445.85	-98.25	-96.8	Q4(3Si,1Al)
T2m		441.41	-93.81	-92.6	Q4(2Si,2Al)
			Ussingite, ordered structure		
T2		445.28	-97.68		Q4(3Si,1Al)
T3		435.54	-87.94	-87.94	Q3(2Si,1Al)
T4		431.16	-83.56		Q3(1Si,2Al)
			Ussingite, disorder model 1		
T1	33	449.22	-101.62	-98.7	**Q4(3Si,1Al)**
All Si in T2 (15 sites):					
T2	mean	445.68	-98.08	-96.5	Q4(3Si,1Al)
	maximum	446.98	-97.31		
	minimum	444.91	-99.38		
T3	65	440.12	-92.52	-91.6	**Q3(3Si)**
T3	68	433.29	-85.69	-85.5	**Q3(1Si,2Al)**
T3	77	432.18	-84.58	-85.0	**Q3(1Si,2Al)**
T3	66	436.94	-89.34	-89.3	Q3(2Si,1Al)
T3	73	436.03	-88.43	-88.6	Q3(2Si,1Al)
All Si in T3 of Q^3(2Si,1Al) (i.e., all Si in T3 except 65,68,77) (13 sites):					
T3	mean	435.76	-88.16	-87.9	Q3(2Si,1Al)
	maximum	436.94	-87.62		
	minimum	435.22	-89.34		
T4	81	437.09	-89.49	-88.6	**Q3(2Si,1Al)**
T4	89	427.17	-79.57	-81.0	**Q3(3Al)**
T4	90	435.74	-88.14	-87.9	**Q3(2Si,1Al)**
T4	85	431.15	-83.55	-83.3	Q3(1Si,2Al)
T4	92	430.48	-82.88	-83.1	Q3(1Si,2Al)
All Si in T4 of Q^3(1Si,2Al) (i.e., all Si in T4 except 81,89,90) (13 sites):					
T4	mean	431.18	-83.58	-84.1	Q3(1Si,2Al)
	maximum	431.81	-82.88		
	minimum	430.48	-84.21		

[a] σ_i^{Si}: ^{29}Si isotropic shielding; δ_i^{Si}, calc: calculated ^{29}Si isotropic chemical shift referenced to the experimental value (δ_i^{Si}, exp) for the narrow peak near -87.94 ppm of ussingite, i.e., $\delta_i^{Si} = -87.94+435.54-\sigma_i^{Si}$.

[b] Experimental data for albite from Sanchez-Munoz et al., 2022. ^{29}Si peaks in experimental data of ussingite assigned according to the order of chemical shift in ^{1}H-^{29}Si HETCOR.

[c] Bold letters highlight T1 site occupied by Si, and T3 and T4 sites whose NNN are different from that of the ordered structure.

This is the peer-reviewed, final accepted version for American Mineralogist, published by the Mineralogical Society of America.
The published version is subject to change. Cite as Authors (Year) Title. American Mineralogist, in press.
DOI: https://doi.org/10.2138/am-2023-9008. http://www.minsocam.org/

879

880 Table 8. ^{27}Al NMR parameters from first-principles calculation

Al site	σ_i^{Al} (ppm)[a]	δ_i^{Al}(ppm) [a]	C_Q^{Al} (MHz) [b]	η_Q^{Al}	δ_1^{Al} (ppm) [c]
Low albite					
Al	515.36	63.00	2.04	0.53	
Ussingite, ordered structure					
Al	518.28	60.08	3.67	0.89	65.60
Ussingite, disorder model 1					
Al in T1 (16 sites):					
mean	518.22	60.14	3.75	0.82	65.78
maximum	518.83	60.81	4.43	0.98	68.20
minimum	517.55	59.53	3.10	0.59	63.42
Al in T2	516.42	61.94	3.62	0.74	66.97

[a] σ_i^{Al}: ^{27}Al isotropic shielding; δ_i^{Al}: ^{27}Al isotropic chemical shift using low albite as a secondary reference, i.e., $\delta_i^{Al} = 63.0+515.36-\sigma_i^{Al}$. The experimental data of low-albite (δ_i^{Al}: 63.0 ppm; C_Q^{Al}: 3.22 MHz; η_Q^{Al}: 0.65) from Sanchez-Munoz et al. (2022) are used for δ_i^{Al} referencing.
[b] For C_Q^{Al}, only the absolute values are shown.
[c] δ_1^{Al}: peak position in the isotropic (F_1) dimension of 3QMAS NMR spectrum expected.

881

882

883 Table 9. ^{23}Na NMR parameters from first-principles calculation

Na site	σ_i^{Na} (ppm)[a]	δ_i^{Na}(ppm)[a]	C_Q^{Na} (MHz)[b]	η_Q^{Na}	δ_l^{Na} (ppm)[c]
		Low albite			
albite	569.07	-8.95	2.42	0.54	
		Ussingite, ordered structure			
Na1	560.61	-0.49	2.21	0.98	8.02
Na2	554.85	5.27	2.27	0.62	12.91
		Ussingite, disorder model 1			
Na1 sites (16):					
mean	560.52	-0.40	2.39	0.81	8.80
maximum	563.32	3.80	3.43	0.99	19.39
minimum	556.32	-3.20	2.05	0.17	4.71
Na2 sites (16):					
mean	555.50	4.63	2.28	0.61	12.39
maximum	559.92	7.29	2.44	0.92	16.90
minimum	552.83	0.20	1.99	0.30	8.85

[a] σ_i^{Na}: ^{23}Na isotropic shielding; δ_i^{Na}: ^{23}Na isotropic chemical shift using low albite as a secondary reference, i.e., $\delta_i^{Na} = -8.95+569.07-\sigma_i^{Na}$. For comparison, the experimental data of low albite derived from NMR spectra at two magnetic fields of 9.4 and 19.6 T by Sanchez-Munoz et al. (2022) are δ_i^{Na}: -8.7~-9.2 ppm; C_Q^{Na}:2.59~2.64 MHz; η_Q^{Na}: 0.25~0.28. The average experimental δ_i^{Na} value was used for referencing.

[b] For C_Q^{Na}, only the absolute values are shown.

[c] δ_l^{Na}: peak position in the isotropic (F_1) dimension of 3QMAS NMR spectrum expected.

884

885

This is the peer-reviewed, final accepted version for American Mineralogist, published by the Mineralogical Society of America.
The published version is subject to change. Cite as Authors (Year) Title. American Mineralogist, in press.
DOI: https://doi.org/10.2138/am-2023-9008. http://www.minsocam.org/

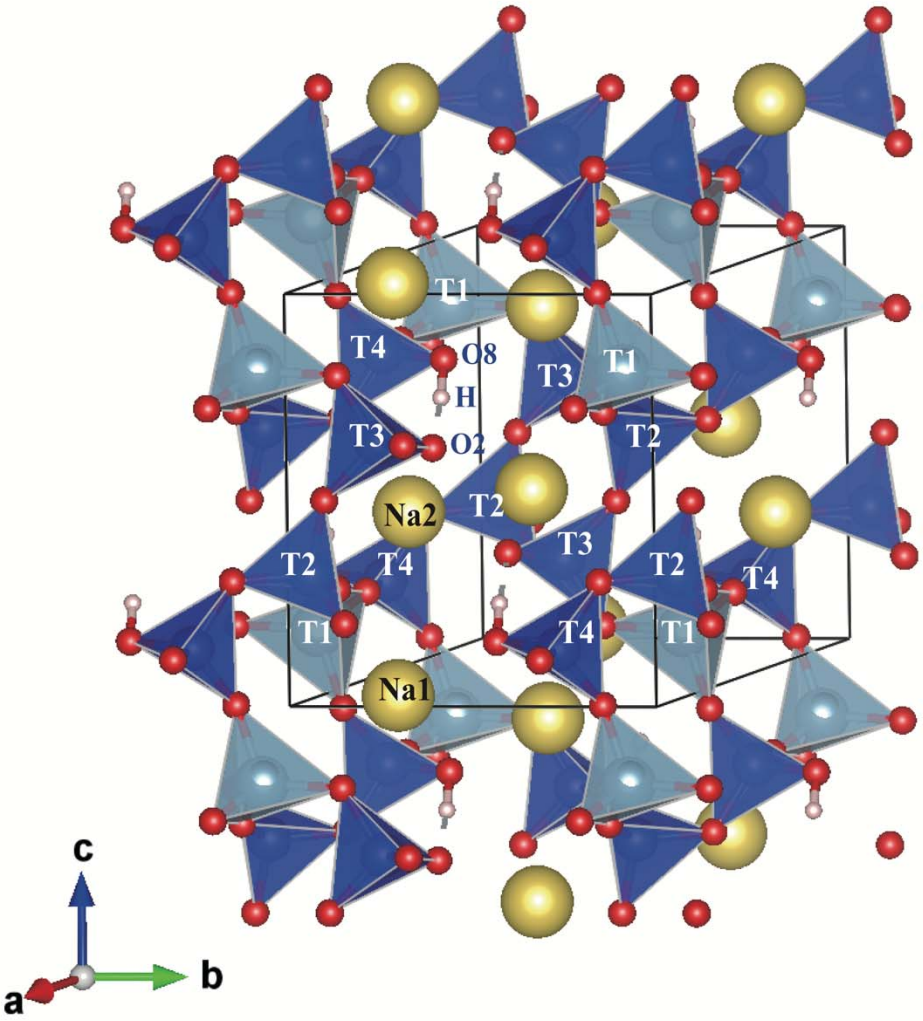

Fig. 1

This is the peer-reviewed, final accepted version for American Mineralogist, published by the Mineralogical Society of America.
The published version is subject to change. Cite as Authors (Year) Title. American Mineralogist, in press.
DOI: https://doi.org/10.2138/am-2023-9008. http://www.minsocam.org/

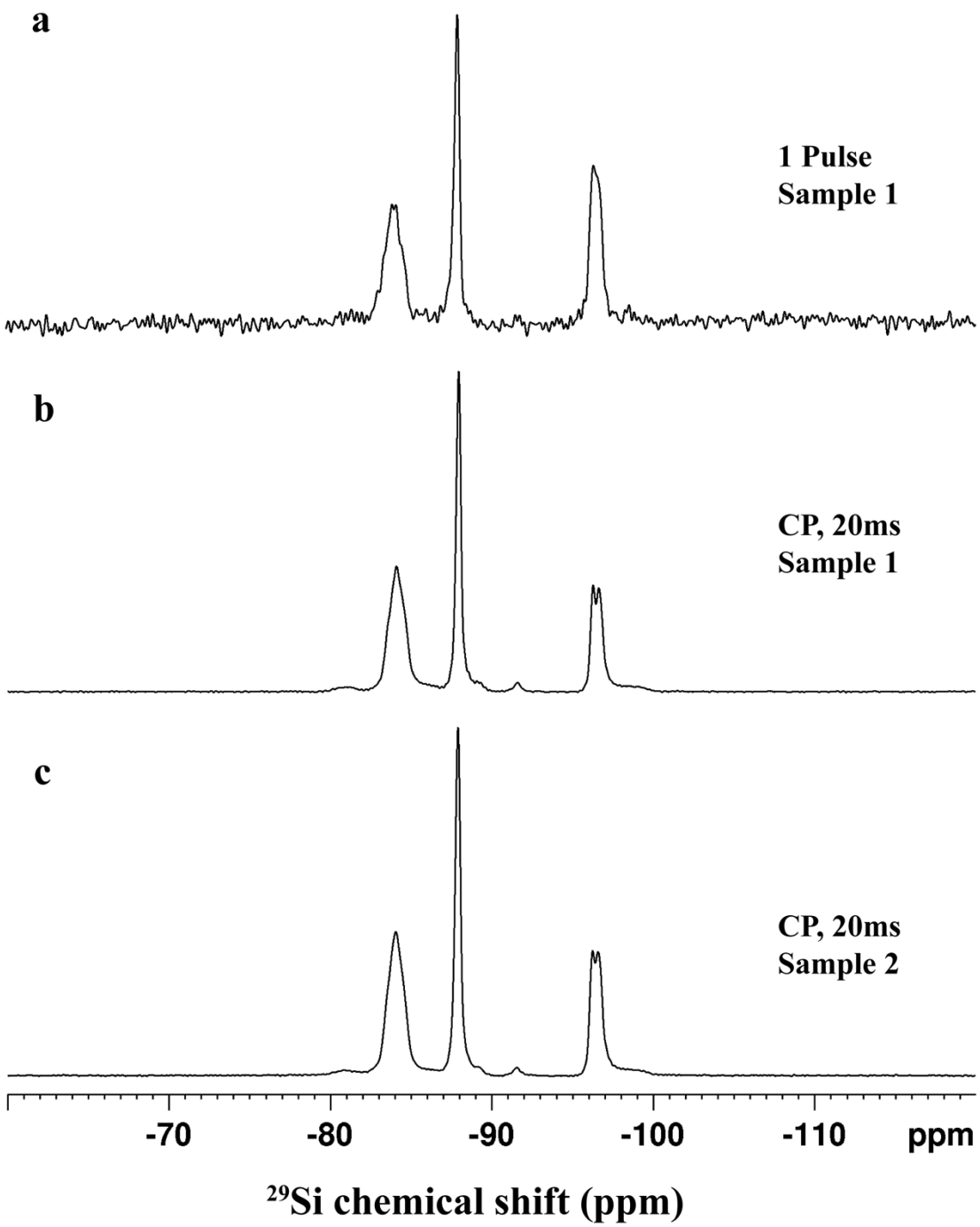

Fig. 2

This is the peer-reviewed, final accepted version for American Mineralogist, published by the Mineralogical Society of America.
The published version is subject to change. Cite as Authors (Year) Title. American Mineralogist, in press.
DOI: https://doi.org/10.2138/am-2023-9008. http://www.minsocam.org/

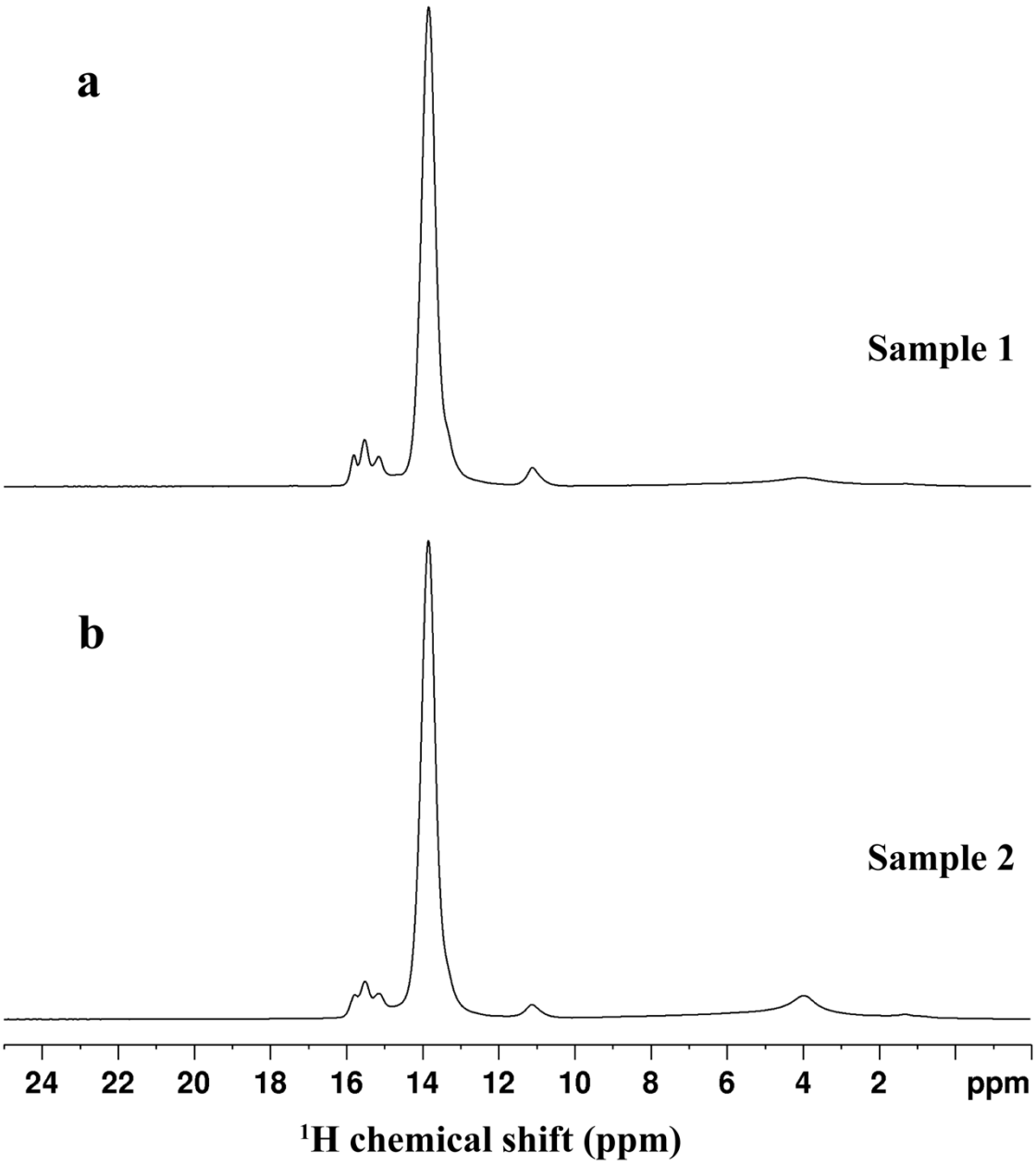

Fig. 3

892
893

This is the peer-reviewed, final accepted version for American Mineralogist, published by the Mineralogical Society of America.
The published version is subject to change. Cite as Authors (Year) Title. American Mineralogist, in press.
DOI: https://doi.org/10.2138/am-2023-9008. http://www.minsocam.org/

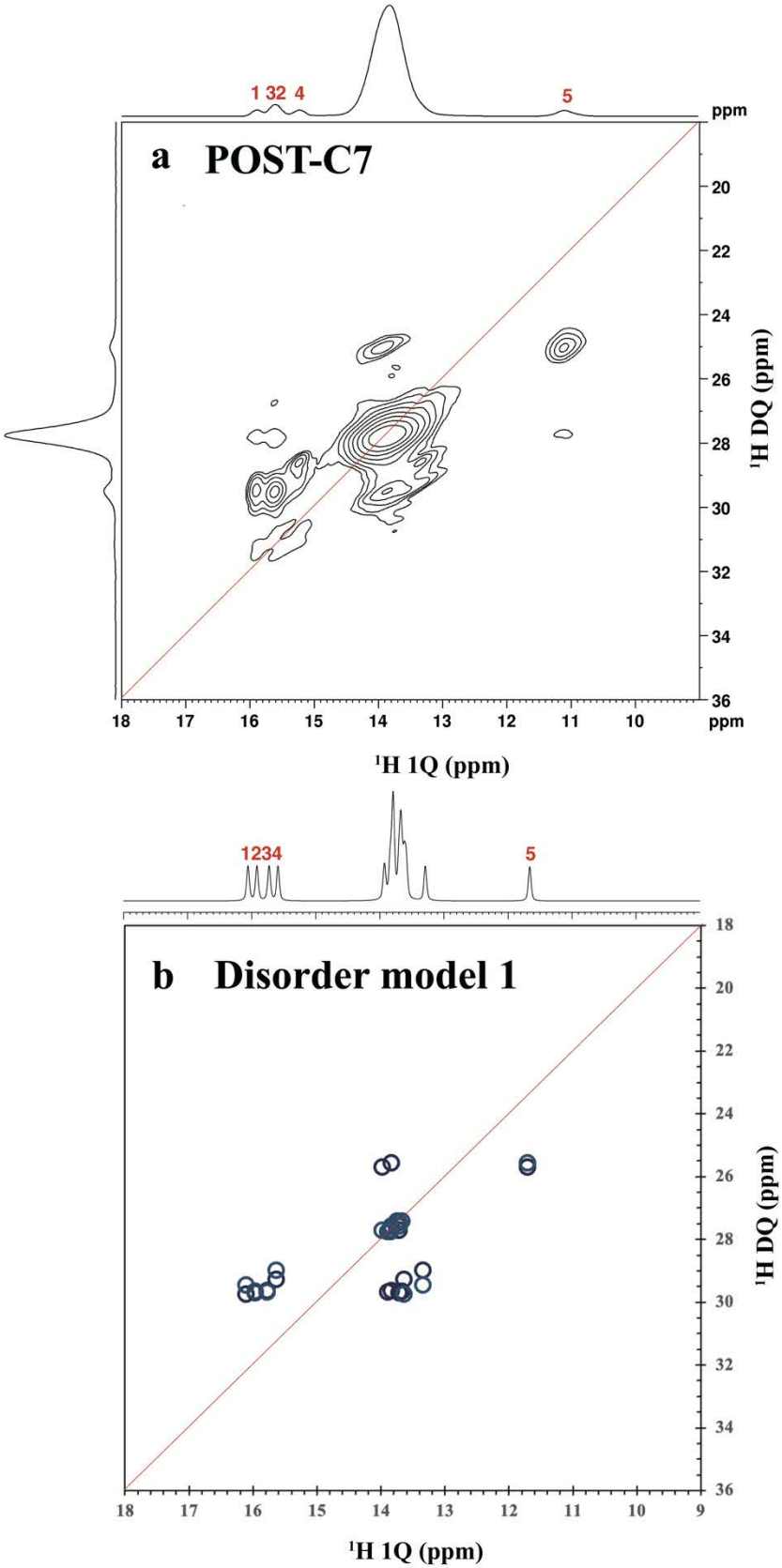

Fig. 4

894

This is the peer-reviewed, final accepted version for American Mineralogist, published by the Mineralogical Society of America.
The published version is subject to change. Cite as Authors (Year) Title. American Mineralogist, in press.
DOI: https://doi.org/10.2138/am-2023-9008. http://www.minsocam.org/

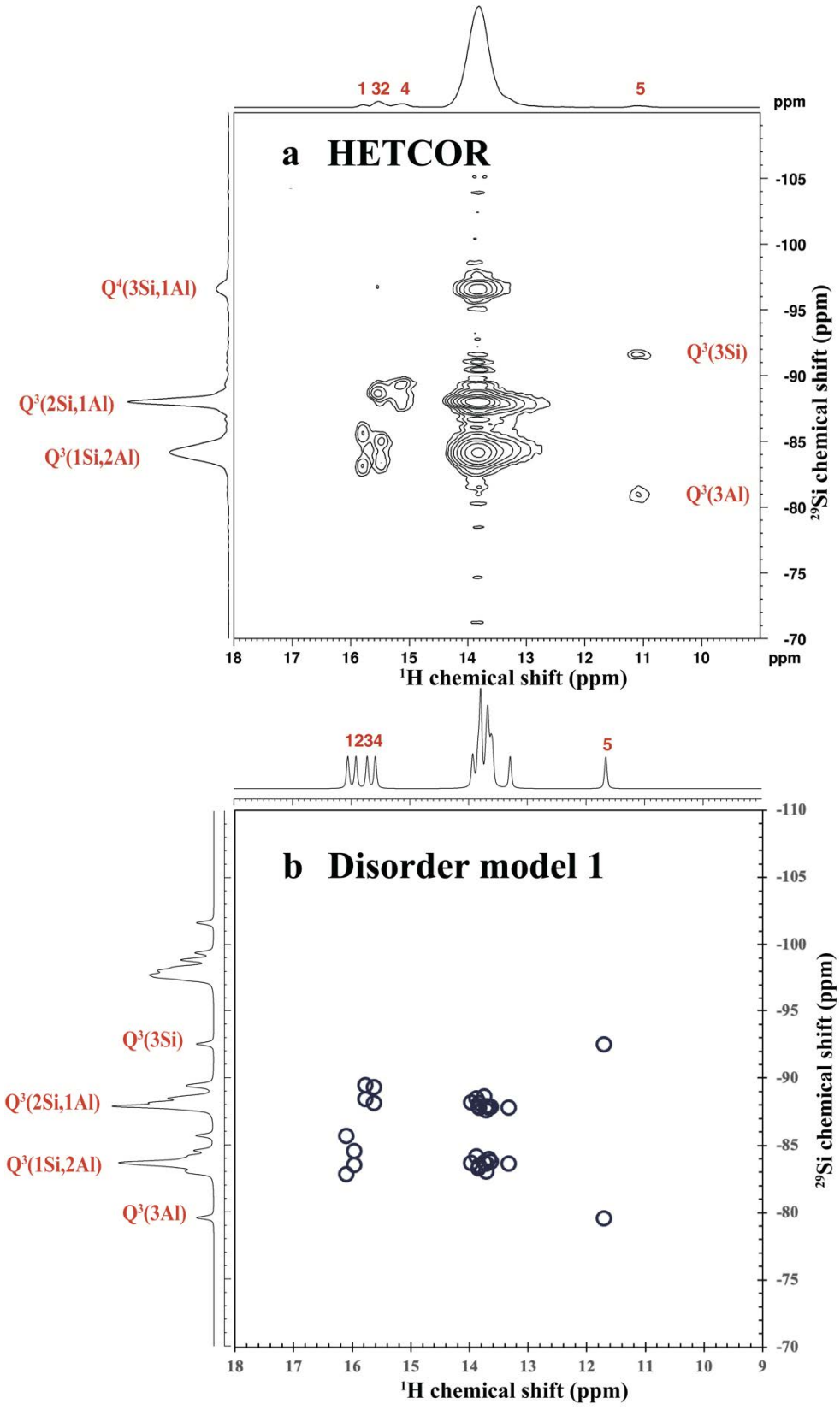

Fig. 5

This is the peer-reviewed, final accepted version for American Mineralogist, published by the Mineralogical Society of America.
The published version is subject to change. Cite as Authors (Year) Title. American Mineralogist, in press.
DOI: https://doi.org/10.2138/am-2023-9008. http://www.minsocam.org/

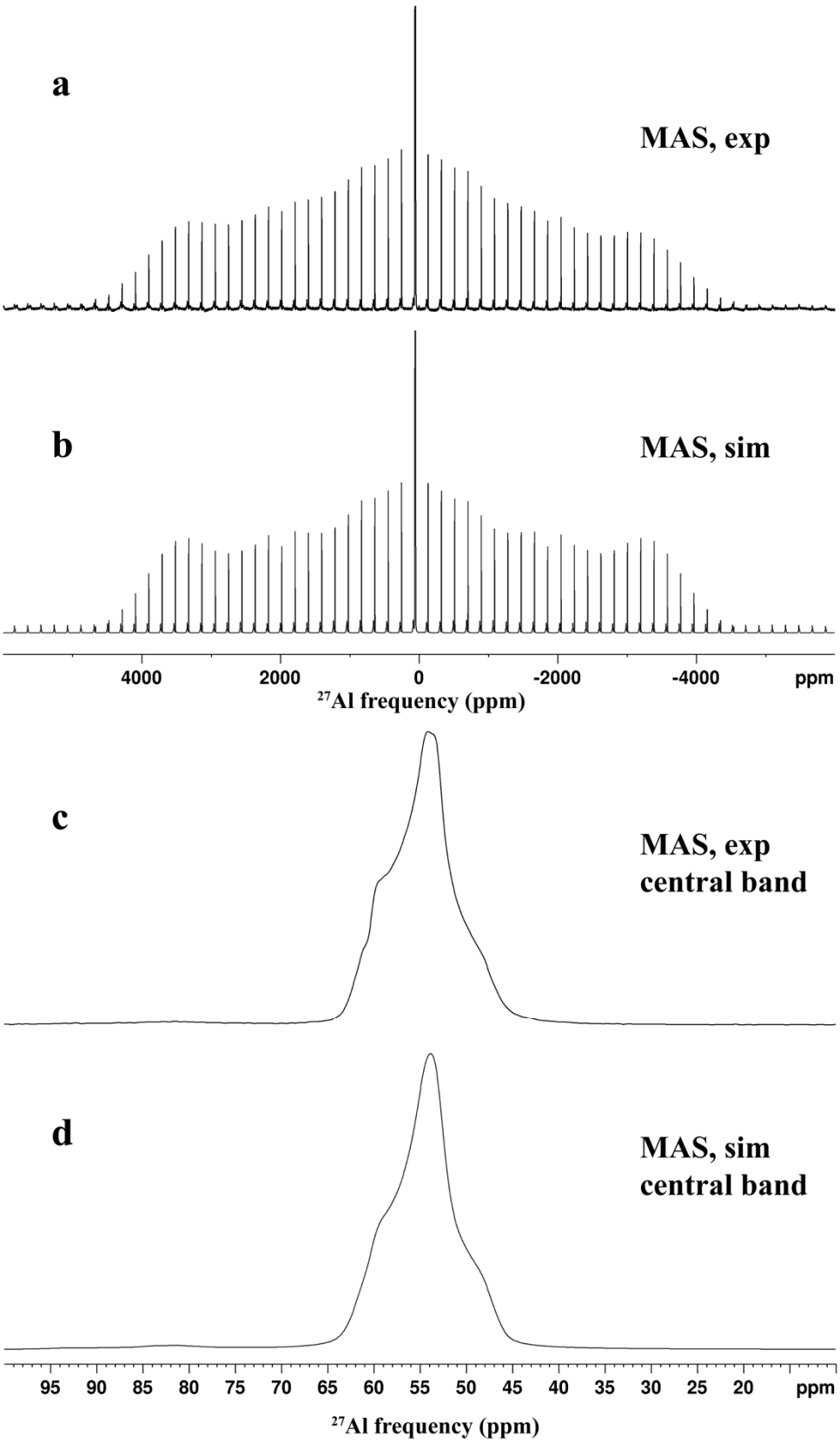

896 **Fig. 6**

This is the peer-reviewed, final accepted version for American Mineralogist, published by the Mineralogical Society of America.
The published version is subject to change. Cite as Authors (Year) Title. American Mineralogist, in press.
DOI: https://doi.org/10.2138/am-2023-9008. http://www.minsocam.org/

897
898
899

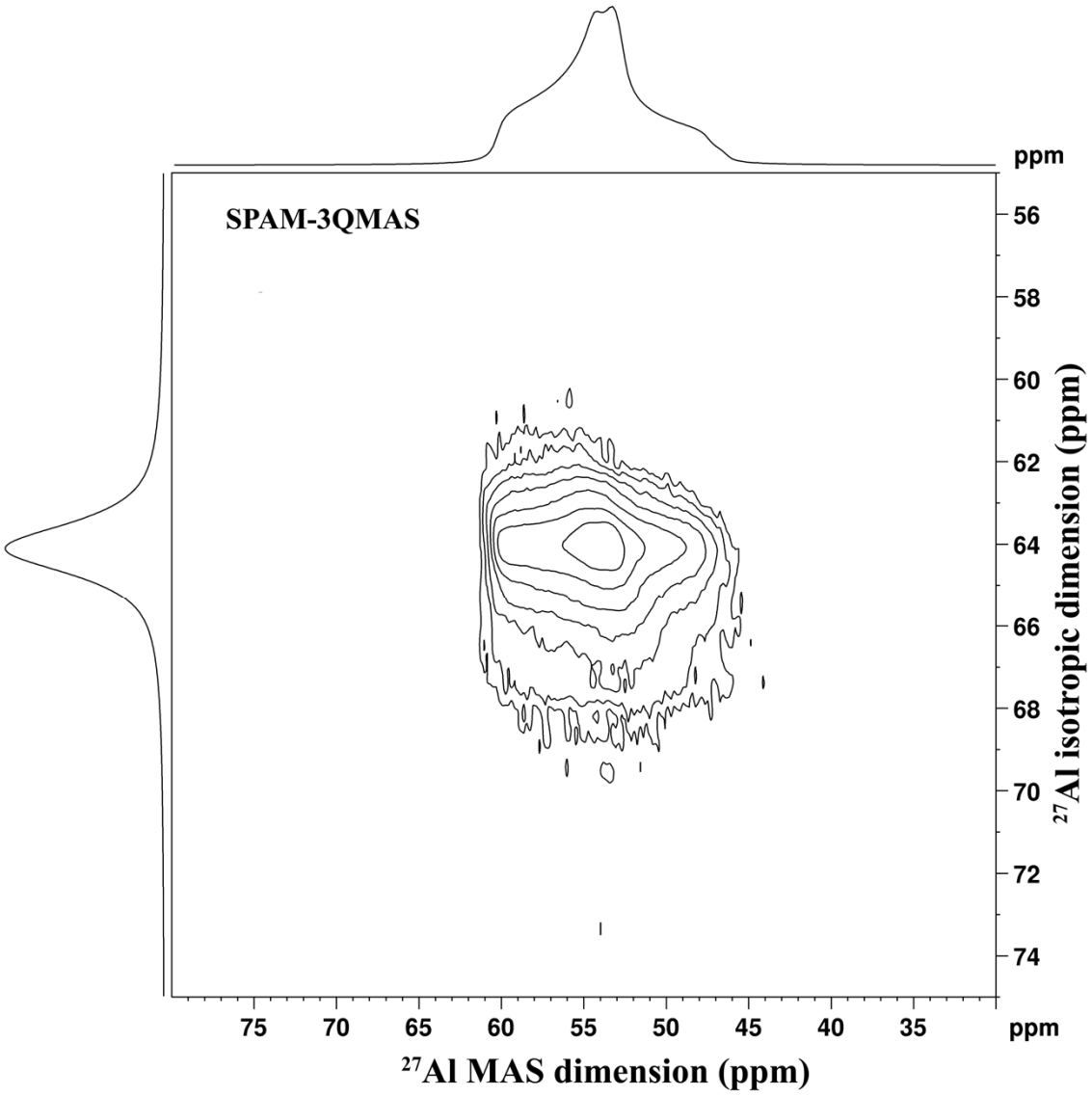

900 **Fig. 7**
901
902

This is the peer-reviewed, final accepted version for American Mineralogist, published by the Mineralogical Society of America.
The published version is subject to change. Cite as Authors (Year) Title. American Mineralogist, in press.
DOI: https://doi.org/10.2138/am-2023-9008. http://www.minsocam.org/

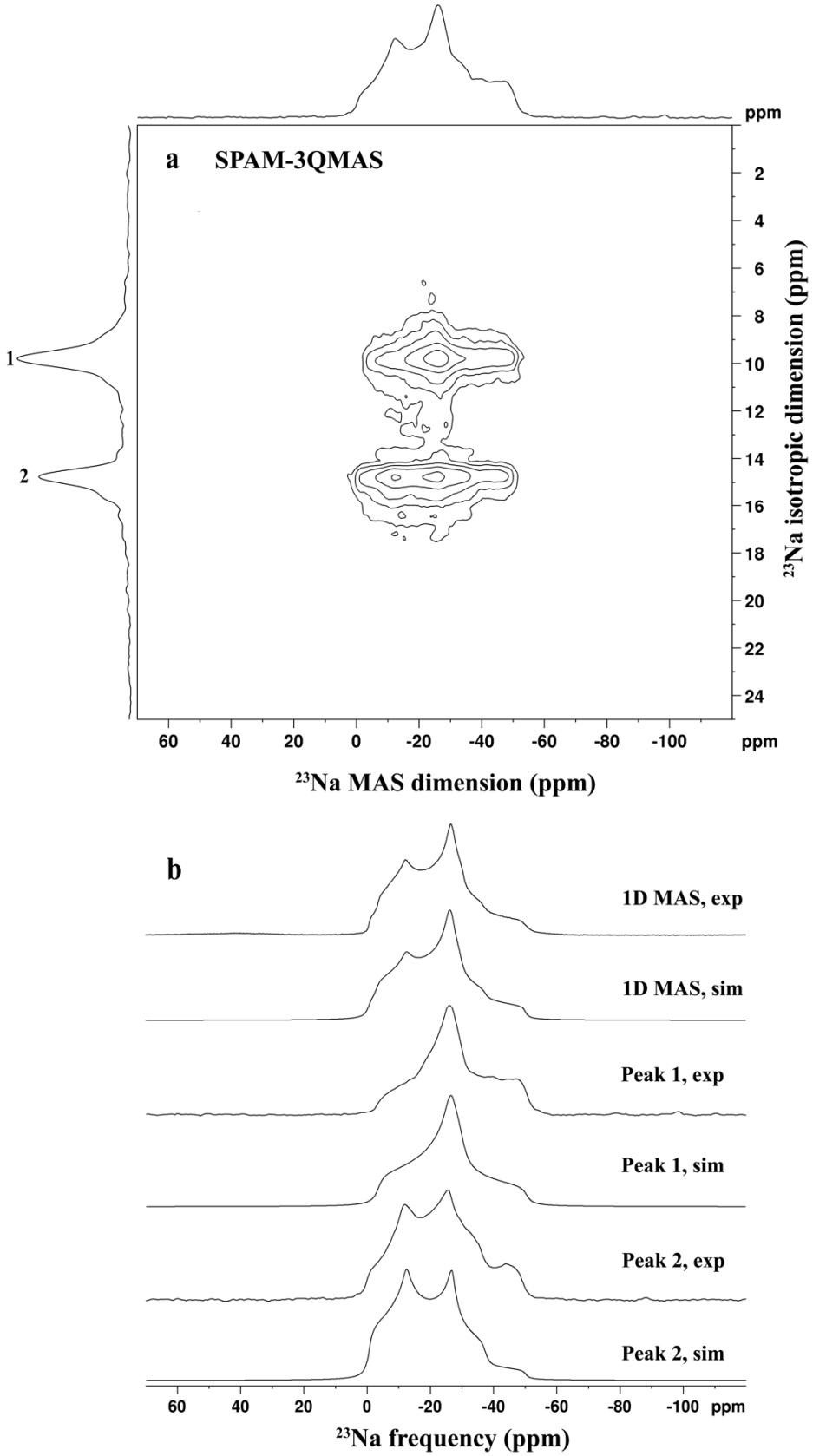

Fig. 8

This is the peer-reviewed, final accepted version for American Mineralogist, published by the Mineralogical Society of America.
The published version is subject to change. Cite as Authors (Year) Title. American Mineralogist, in press.
DOI: https://doi.org/10.2138/am-2023-9008. http://www.minsocam.org/

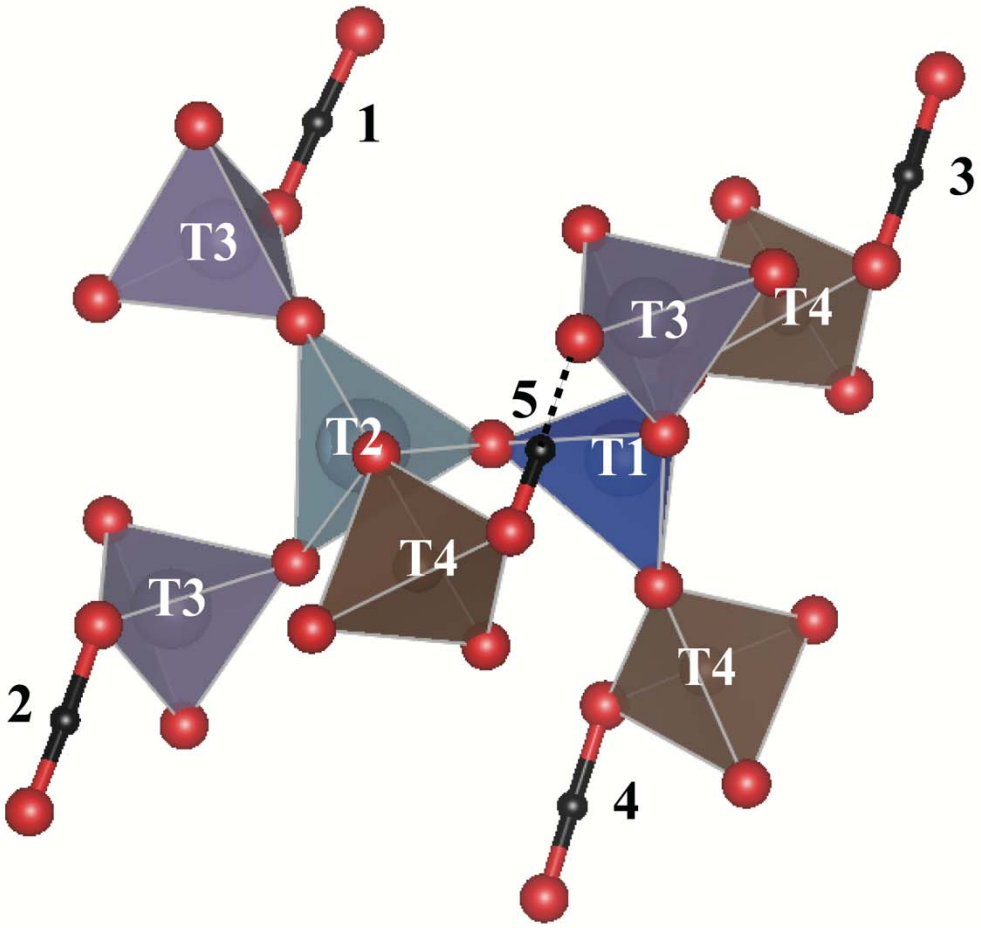

Fig. 9

This is the peer-reviewed, final accepted version for American Mineralogist, published by the Mineralogical Society of America.
The published version is subject to change. Cite as Authors (Year) Title. American Mineralogist, in press.
DOI: https://doi.org/10.2138/am-2023-9008. http://www.minsocam.org/

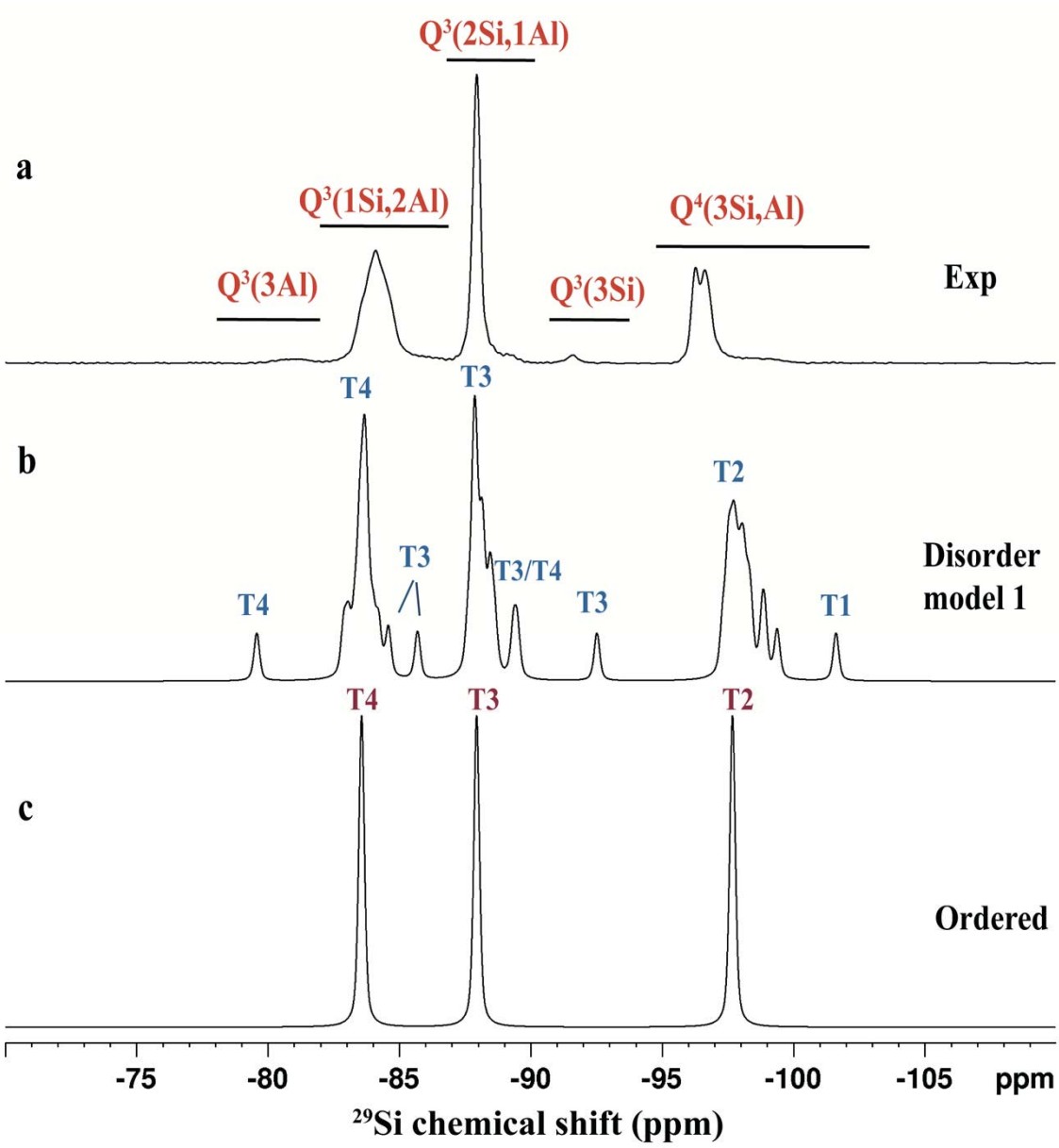

Fig. 10

This is the peer-reviewed, final accepted version for American Mineralogist, published by the Mineralogical Society of America.
The published version is subject to change. Cite as Authors (Year) Title. American Mineralogist, in press.
DOI: https://doi.org/10.2138/am-2023-9008. http://www.minsocam.org/

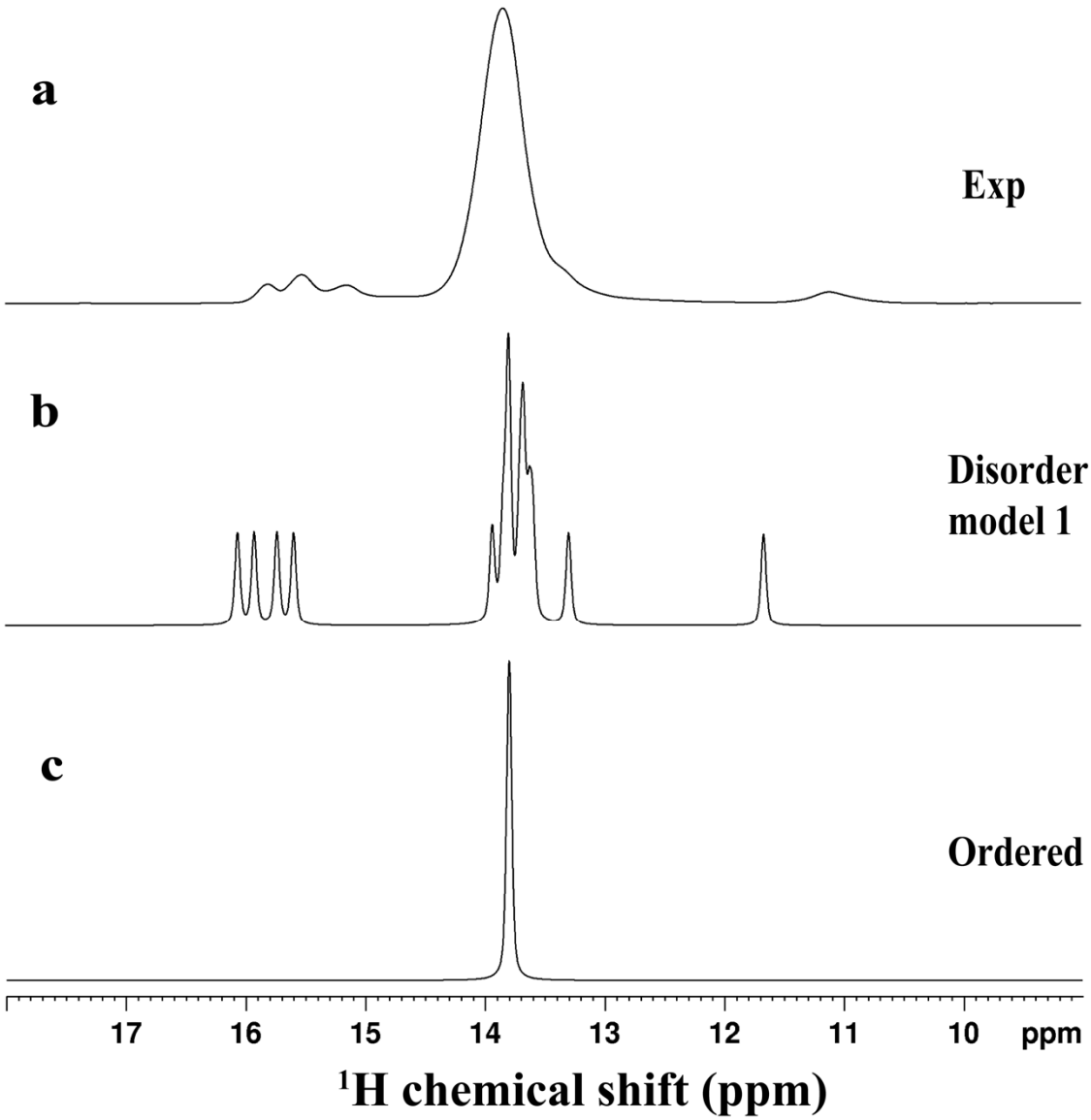

Fig. 11

This is the peer-reviewed, final accepted version for American Mineralogist, published by the Mineralogical Society of America.
The published version is subject to change. Cite as Authors (Year) Title. American Mineralogist, in press.
DOI: https://doi.org/10.2138/am-2023-9008. http://www.minsocam.org/

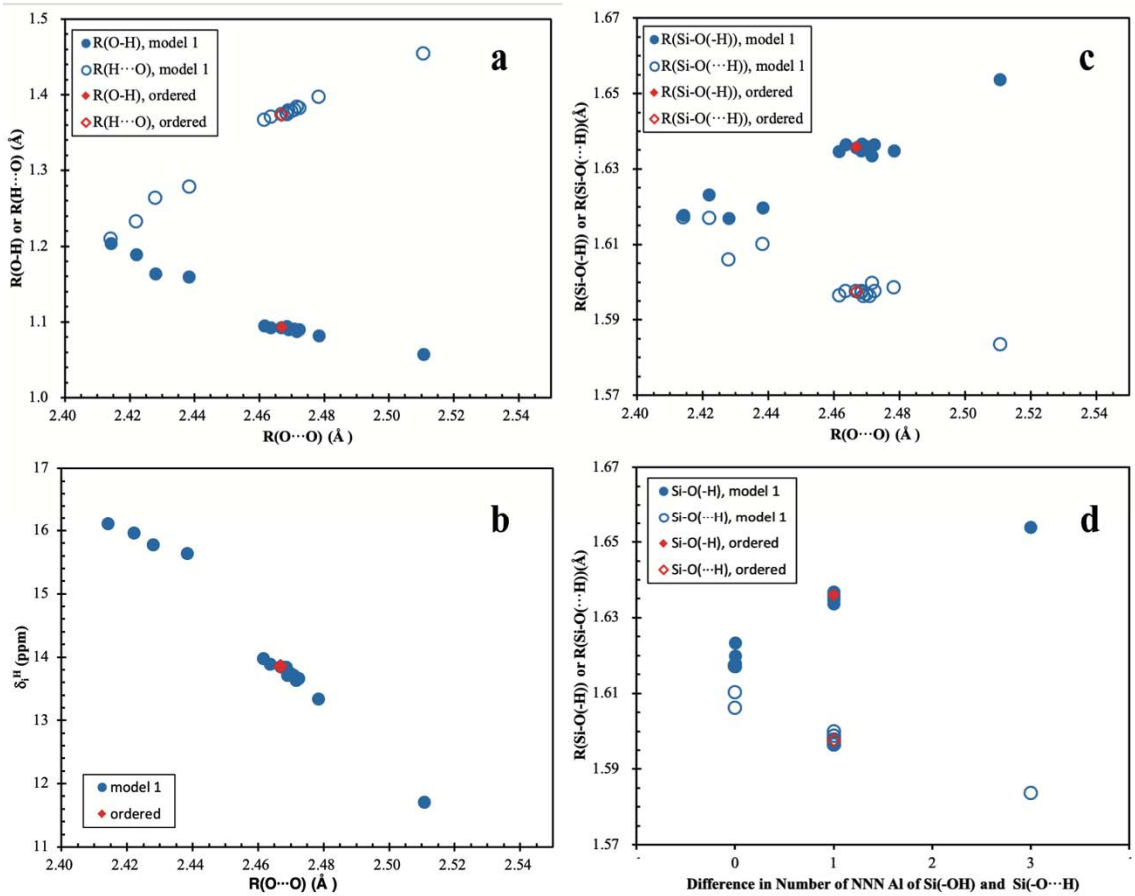

Fig. 12